Magnetocuring of temperature failsafe epoxy adhesives

Chaudhary, Richa; Chaudhary, Varun; Ramanujan, Raju V.; Steele, Terry W. J.

2020

https://hdl.handle.net/10356/144222

https://doi.org/10.1016/j.apmt.2020.100824

1 **Magnetocuring of Temperature Failsafe Epoxy Adhesives**

2 Richa Chaudhary, Varun Chaudhary, Raju V. Ramanujan, Terry W. J. Steele

3

4 School of Materials Science and Engineering (MSE), Division of Materials Technology,

5 Nanyang Technological University (NTU), Singapore 639798

6 Corresponding author: Terry W. J. Steele (e-mail: wjsteele@ntu.edu.sg)

7
8
9 **Abstract:** Adhesive technology is of high and increasing interest in a wide variety of

10 conventional and emerging applications. One-component adhesives typically cure using

11 moisture, heat and light. These approaches limit applications to specific substrates, inefficient

12 handling in manufacturing, and can only be indirectly activated. Hence, we developed a method

13 for remote, wireless, contactless curing of adhesives using alternating magnetic fields (AMF).

14 This approach ("magnetocuring") offers energy efficient, on-demand adhesion. Exposure of

15 $Mn_xZn_{1-x}Fe_2O_4$ Curie temperature tuned magnetic nanoparticles (CNP) additives within

16 commercial epoxy adhesives to an AMF cured thermoset resins within min with minimal rise

17 in substrate temperature. The heating of the CNP "switches off" above its Curie temperature

18 offering failsafe heating. The *in-situ* heating of the CNP can be controlled by CNP composition,

19 CNP loading, and AMF strength. Internal temperatures of 160 °C could be reached in 5 min,

20 allowing curing of most commercial epoxy adhesives without resin scorching. The maximum

21 lap shear adhesion strength exceeded 6.5 MPa. Magnetocuring is demonstrated on wood,

22 ceramics, and plastics, which is of considerable interest in sports, automotive, and aerospace

23 industries.

24 **Keywords:** Adhesives, Alternating magnetic field, Curie nanoparticles, Epoxy, Ferrites,

25 Magnetocuring

26

27

28

1. Introduction

Chemical curing adhesives (CCA) are preferred over mechanical fixation due to their light weight and stress distributed bonding which is free of substrate damage. The global market of instant curing adhesive is expected to be more than $ 3 billion USD[1] by 2023 and is dominated by two-part, thermosetting structural adhesives.[2] Structural adhesives require mixing of epoxy/hardener resins or thermal activation of one-pot epoxy/hardener blends (thermocuring), which leads to energy losses and stress/strain mismatches due to non-uniform temperature cycling of the substrates and resin. Attempts to overcome these impediments have led to alternative methods such as snap-cure epoxy[3-5], photocuring[6, 7], electron beam curing[8], and electrocuring.[9-12]

Snap-cure thermosets are one pot adhesives that rapidly cure within min. However, the rapid curing nature is of limited benefit to insulating or heat-sensitive materials (e.g., wood, ceramics, or plastics).[13] Photocuring offers non-contact activation, but is dependent on UV transparent materials and free radical initiators, which contribute to manufacturing problems of dermal sensitivity.[14] Electron beam curing works by impinging high speed electrons that initiate free radicals within the polymer-initiator. The high energy of the electron beams/ radiation penetrates offers uniform curing, but requires high capital and infrastructure investments. All parts must be electron irradiated, which requires shielded rooms and advanced technical personnel.[15, 16] Surface-curing adhesive is methyl/ethyl-cyanoacrylate, also known as 'Superglue'. It has the unique property of either forming strong substrate bonds or not bonding at all. The inability to bond rough/acidic surfaces, the difficulty in handling brittle materials, and unsatisfactory temperature stability (cured bonds must be kept $< 70°C$) limits surface curing to do-it-yourself home repairs.[17]

Alternating magnetic field (AMF) mediated adhesive curing ('magnetocuring') occurs by in situ activation of thermoset adhesives. It is a non-contact method of bonding non-metal

materials. Previous studies have investigated magnetocuring based on FeCo epoxy composties.[18] Induction curing of thiol-acrylate and thiol-ene composite systems using cobalt and nickel particles has been demonstrated.[19] Polymerization of cyanate ester using Fe_3O_4 as an internal heat source through induction heating was studied.[20] Induction curing was also studied with nickel nanoparticles for bonding of composites[21] and polymerization using iron oxide nanochains.[22] However these formulations were never successfully commercialized due to the follwing limitations: (i) absence of surface functionalization leads to poor colloidal stability of the magnetic nanoparticles. This would prevent adequate shelf stability due to the formation of large aggregates (ii) nanoparticle aggregates lead to thermal hotspots and localized resin/epoxy pyrolysis,[18] (iii) high power input (3-32 kW)[19] paired with inefficient metallic Co (2 μm) and Ni (3 μm) particles[20] or Fe_3O_4 particles,[22] (iv) use of high frequency (>2 MHz) and broad particle size distribution (70 nm – 22 μm).[21]

To overcome these limitations, colloidal stability and aggregate induced hotspots needs to be addressed. Herein, it is hypothesized that surface functionalized magnetic nanoparticles (CNP) will serve as magnetocuring additives within thermoset resins. This allows one-pot adhesive formulations that activate substrate bonding and adhesive crosslinking upon exposure to AMF. The bonding initiation can be precisely tuned to the Curie nanoparticle cutoff temperature with optimized heating, allowing bonding to heat-sensitive substrates while eliminating scorching. In order to support the hypothesis, following steps were carried out: (1) $Mn_xZn_{1-x}Fe_2O_4$ CNP will be synthesized by a facile hydrothermal method with controlled particle size (< 20 nm) and Curie temperature (Tc). The Curie temperature of $Mn_xZn_{1-x}Fe_2O_4$ ferrites can be tuned by changing the ratio of Mn to Zn content. (2) Organic coatings and surface functionalization on CNP with oleic acid and bisphenol A diglycidyl ether was used to overcome previous laboratory failures with long term CNP colloidal stability in liquid epoxy/adhesives. (3) Incorporation of CNP into adhesives and optimal AMF induction (low

79 power system) that allows snap-curing formulations while preventing substrate hotspots and

80 scorching. (4) Lastly, the loading of CNP, thermal and physical properties of adhesives,

81 selection of substrates will allow tuning of mechanical properties and shear adhesion strength.

82 CNP offers a prime advantage over other magnetic nanoparticles due to its failsafe

83 temperature limits. This is the major rationale for choosing them for magnetically induced

84 heating and activation of thermoset epoxy adhesives. For the first time, CNP have been

85 employed to cure one component epoxy adhesives through a non-contact modifier

86 methodology. The modifier methodology allows its incorporation into already commercialized

87 thermoset adhesive formulations. Magnetocuring offers a more cost-effective activation

88 method, since the adhesive is heated directly without substrate thermal conduction. Here,

89 curing of one-component epoxy adhesives through AMF activation or 'magnetocuring' is

90 demonstrated on wood, ceramics, and plastics, which is of significant interest in sports,

91 automotive, and aerospace industries.

92 The novelty of the present work includes i) development of several temperature fail

93 safe magnetoadhesives using commercial one component adhesives, ii) proof of concept to join

94 a range of materials using magnetoadhesive under AMF, these materials are close to

95 impossible to join using a conventional oven method, iii) Our approach of curing is remotely

96 controlled, rapid and localized heating, reduced processing cost and energy and absence of

97 scorching.

98

99 **2. Materials and Methods**

100 **2.1. Materials**

101 One component epoxy adhesives (ES558 Permabond and TIM-813HTC-1HP) are purchased

102 from Permabond, USA and TIMTRONICS, USA, respectively. The divalent manganese (II)

103 chloride tetrahydrate ($MnCl_2 \cdot 4H_2O$, 99%), zinc chloride, anhydrous ($ZnCl_2$, 98%) and trivalent

104   iron (III) chloride hexahydrate ($FeCl_3 \cdot 6H_2O$), oleic acid (OA), bisphenol A diglycidyl ether

105   (BADGE) and dicyanamide (DICY) are purchased from Sigma Aldrich and used as received.

106   Wood popsicle sticks and polymethyl methacrylate (PMMA) sheets are purchased from Art

107   Friend, Singapore. Acrylonitrile butadiene styrene (ABS-100) used for 3D printing is

108   purchased from Additive 3D Asia, Singapore. Microscope slides, borosilicate (25.4 mm x 76.2

109   mm, thickness 1-1.2 mm) are purchased from Newton 101 PTE. LTD. Singapore.

110

111   **2.2. Methods**

112   **2.2.1. Synthesis of Magnetocuring Adhesive Modifier Curie Nanoparticles (CNP)**

113   Magnetocuring additives, CNP of composition $Mn_xZn_{1-x}Fe_2O_4$ (x = 0.4, 0.5, 0.6 and 0.7) are

114   synthesized using a modified hydrothermal method.[23, 24] Briefly, for the synthesis of a 4 g

115   batch $Mn_{0.7}Zn_{0.3}Fe_2O_4$ particles, 10 mL solutions of 70 mmol $MnCl_2 \cdot 4H_2O$ (2.22 g) and

116   30 mmol $ZnCl_2$ (0.654 g) are prepared separately in distilled water (DI water). 200 mmol of

117    $FeCl_3 \cdot 6H_2O$ (8.64 g) is dissolved in 40 mL DI water and NaOH (4M) solution is added

118   dropwise until the pH value reached at 8. The resulting brown precipitate is centrifuged and

119   washed three times with DI water, and transferred to a beaker equipped with a mechanical

120   stirrer. The separately prepared Mn and Zn salt solutions are then added together into the beaker

121   and the mixed solution is stirred vigorously while adding NaOH solution dropwise until the

122   pH value of the reaction mixture reached 12. This resulting slurry is decanted into a Teflon-

123   lined stainless-steel autoclave (4748A Parr, USA) and placed in an oven at 190 °C for 2 h. The

124   resulting nanoparticles is washed three times with DI water and two times with ethanol (96%),

125   followed by vacuum drying for 48 h. 95 % yield of vacuum dried particles is obtained. All

126   other CNP ($Mn_{0.4}$, $Mn_{0.5}$ and $Mn_{0.6}$) are also synthesized in a similar fashion with 95-97% yield

127   and stored under vacuum. Prior to further modification, all the synthesized CNP are

128 characterized for their structural, functional and magnetic properties using XRD, ICP-MS,

129 TGA, FTIR, and PPMS.

130

131 **2.2.2. Surface Modification of Curie Nanoparticles with Oleic Acid (OA)**

132 CNP are coated with oleic acid to prevent agglomeration. 2 g of CNP are dispersed in 80 mL

133 of deionized water and placed in a sonicating water bath (Elmasonic S 60 H, Germany) for 20

134 min. to break up the aggregates. 4 mL of OA is added to the solution and sonicated for 10 min.

135 This solution is heated at 80 °C for 1 h under mechanical stirring at 400 rpm. The resultant

136 solution is washed 3-4 times with ethanol, the OA coated CNP are separated using a permanent

137 magnet. The oleic acid coated particles are modified with bisphenol A diglycidyl ether.

138

139 **2.2.3. Surface Modification of $Mn_xZn_{1-x}Fe_2O_4$/OA with Bisphenol A Diglycidyl Ether**

140 **(BADGE)**

141 $Mn_xZn_{1-x}Fe_2O_4$/OA particles from the first step are dispersed into 10 mL of tetrahydrofuran

142 (THF) and sonicated for 30 min. A solution of 10 g bisphenol A diglycidyl ether (BADGE) in

143 20 mL THF is added to the above solution and sonicated again for 30 min. This solution is kept

144 for 16 h until the surface of nanoparticles is completely wetted with BADGE. This consequent

145 solution is washed by tetrahydrofuran and acetone and the $Mn_xZn_{1-x}Fe_2O_4$/OA/epoxy

146 nanocomposites are separated using a permanent magnet followed by vacuum drying for 24 h.

147 On the basis of the dried particles weight, 1.94 g yield for the surface functionalization is

148 observed. The amount of OA and BADGE anchored on the surface of the functionalized

149 particles is determined by thermogravimetric analysis.

150

151

152

153 **2.2.4. Alternating Magnetic Field Heating of Functionalized Curie Nanoparticles**

154 The alternating magnetic field (AMF) generator of D5 series (640W mono frequency F1

155 driver) from nB nanoScale Biomagnetics, Spain is used by incorporating a solenoid coil (S[56])

156 at a fixed frequency of 400 kHz. AMF heating of the CNP dispersed in BADGE for different

157 concentrations (5-30 *wt.%*) are determined at applied magnetic fields ranging from 50 to 140

158 Oe. The temperature under AMF is measured using a fibre optic temperature sensor (Neoptix

159 T1S-01-PT15, USA). All the samples are freshly prepared by dispersing the appropriate

160 amount of CNP into BADGE and treated with ultrasound sonication for 60 min.

161

162 **2.2.5. Specimen Preparation by 3D Printing**

163 All the ABS coupons are printed using a Cubicon 3DP-110F printer. The T-shaped geometry

164 of ABS coupons is created using Solidworks and saved as stereolithographic (STL) file. This

165 STL file is opened in 3D printer software and the Gcode is exported to the printer. The

166 dimensions of ABS coupons and printing parameters are listed in **Table 1**.

167   **Table1.** Dimensions of ABS coupons and parameters used for 3D printing.

Dimensions	Values
Length	90 mm
Width	20 mm
Thickness	3 mm
Printing parameters	
Extruder temperature	240 ^{o}C
Bed temperature	115 ^{o}C
Chamber temperature	45 ^{o}C
Layer Height	0.25 mm

Wall thickness	0.8 mm
Infill	20%

168

2.2.6. Adhesive Curing by AC Magnetic Field

170 Commercially procured Permabond ES558 and TIMTRONICS 813-HTC and a mixture of

171 BADGE and dicyanamide (100:12) are used for magnetocuring of one-component epoxy

172 adhesives. A range of CNP loading (15-30 *wt.%*) with respect to the adhesive/BADGE is used

173 for magnetocuring of wood, glass, PMMA and ABS coupons. Samples are cured at a magnetic

174 field strength of 140 Oe and frequency of 400 kHz .

175

2.2.7. Structural and Magnetic Characterizations of CNP

177 X-ray diffraction (XRD) is carried out with a Bruker D8 Advance powder diffractometer, using

178 Cu-Kα radiation operated at 40 kV and 40 mA, in the range from $2\theta = 20°$ to $70°$, at a scan

179 rate of $5°min^{-1}$. Phase identification is performed by matching diffraction peak positions and

180 relative intensities to reference JCPDS files. The crystallite size is calculated using the Scherrer

181 formula $D = 0.9 \lambda/(\beta \cos \theta)$, where λ is the wavelength of the X-rays (1.54 Å), β is the full

182 width at half maximum (FWHM) of the 311 diffraction peak and θ is the Bragg angle.

183

2.2.8. Elemental Composition of CNP

185 Elemental composition of the CNP is measured by Inductively coupled plasma mass

186 spectrometry (ICP-MS) Agilent 7700, Japan. Samples are prepared by dissolving the particles

187 in a mixture of hydrochloric acid (HCl) and nitric acid (HNO_3) at a ratio of 3:1 followed by the

188 dilution with millipore water. Prior to the analysis, the sample solution is filtered using 0.2 μm

189 pore sized syringe filter (Agilent).

190

2.2.9. Physical Property Measurement of CNP

The magnetic properties of CNP are measured using a physical property measurement system (PPMS) (EverCool-II, Quantum Design, USA), equipped with a vibrating sample magnetometer and an oven (model P527). The room temperature hysteresis curves of the CNP are recorded up to an applied field of 2 T. The magnetization versus temperature curves are measured in the temperature range of room temperature to 600 °C at different applied magnetic fields ranging from 50 Oe to 140 Oe.

2.2.10. Quantification of Coating on the CNP

Thermal degradation of the bare nanoparticles and the amount of OA and BADGE coated on the nanoparticles are measured using thermogravimetric analysis (TGA). TGA is carried out using a TA Instruments TGA Q500 over a temperature range from 30 to 900 °C at a ramp rate of 10 °Cmin^{-1} under nitrogen atmosphere.

2.2.11. Colloidal Stability of CNP

The stability of the CNP are examined by a Zetasizer (Zetasizer Nano, Malvern Instruments, UK) using a 173° backscatter measurement. The colloidal stability of the functionalized nanoparticles dispersed in ethanol is investigated by measuring the mean count rate (kilo count per second, kcps) versus time. 5 mg of CNP ($Mn_xZn_{1-x}Fe_2O_4$/OA/BADGE) are dispersed in 5 mL of ethanol and sonicated for 1 h. For all the samples, ten measurements with ten repeated runs were recorded.

2.2.12. Particle size of CNP

The particle size and morphology of the synthesized and functionalized Curie nanoparticles are characterized using a JEOL 2010 transmission electron microscope operating at 200 kV.

216   Samples are prepared by ultrasonically dispersing a small amount of powder in ethanol placing

217   a drop of the suspension on a holey carbon-coated copper grid. Prior to analysis, samples are

218   dried in vacuum oven overnight. ImageJ image processing software is used to analysed the

219   particle size.

220

221   **2.2.13. Curing Temperature from Differential Scanning Calorimetry**

222   DSC analysis is performed using a simultaneous DSC/TGA system, TA Instrument, SDT

223   Q600. Analysis is carried out from 30 to 600 °C at a ramp rate of 10 °Cmin^{-1}.

224

225   **2.2.14. Confirmation of Curie Nanoparticles Functionalization and Percentage**

226   **Crosslinking**

227   FTIR (Perkin Elmer Frontier) measurements of functionalized CNP are performed using a

228   universal Zn-Se ATR (attenuated total reflection) accessory in the 500-4000 cm^{-1} region. The

229   FTIR spectra of CNP and functionalized CNP is recorded by the KBr pellet method. 3-4 mg of

230   CNP are added into 20 mg of potassium bromide (KBr) and mixed with a mortar pestle. This

231   mixture is used to prepare the pellet with a 13 mm KBr die set by applying 10 tons of pressure

232   via a KBr hydraulic press (Specac, UK). The FTIR measurements of adhesives and cured

233   adhesive are performed with a Universal ATR fixture of a ZnSe crystal. Each measurement is

234   an accumulation of 32 scans with a resolution of 4 cm^{-1}.

235

236   **2.2.15. Lap Shear Adhesion**

237   Magnetocuring is demonstrated on different substrates: glass, wood, ABS and PMMA. 125 mg

238   of adhesives are applied onto the substrate/adherent section area of 1 x 1 cm^2. The thickness of

239   the samples is ~ 0.45 mm (±0.05) on all the substrates. The adherents are tightly gripped

240   together with cello-tape. The Lap shear adhesion tests of the magnetocured samples are

241   performed on a Static Mechanical Tester (Criterion MTS C43, USA) with a 2.5 kN load cell

242   and a testing speed of 3 mm/min.

243

244   **2.2.16. Statistical Analysis**

245   All the experiments are performed in triplicate and data presented here as mean $\pm$ SD (n = 3).

246   Significance is determined by one-way ANOVA with Tukey correction, carried out using

247   OriginPro 2018b 64-bit Software, where $p < 0.05$. (*) is considered to be statistically

248   significant.

249

250   **3. Results**

251   A one-pot adhesive platform is designed for non-contact magnetocuring through exposure to

252   AMF. On applying alternating magnetic field, CNP dissipate the applied magnetic energy into

253   heat mainly by relaxation loss processes (Brown and Neel). The heating ability of these CNP

254   exposed to AMF are quantified by specific absorption rate (SAR) parameter, which is

255   calculated by the heat released in unit time by the unit mass of the CNP. The CNP have the

256   advantage of a upper limit of temperature which is controlled by the Mn/Zn ratio. This

257   temperature control prevents scorching—a detrimental property of other magnetic

258   nanoparticles. The Mn/Zn ratio is tuned through the hydrothermal synthesis feedstock

259   determined. Composition in the range of $Mn_{0.4}Zn_{0.6}$ to $Mn_{0.7}Zn_{0.3}$ are chosen as they span

260   cutoff temperatures of 100-250°C, relevant to most thermoset resins.[25, 26] To prevent

261   aggregation and maximise shelf stability, the bare CNP are surface functionalized with oleic

262   acid and BADGE. Oleic acid (OA) is widely used in nanoparticle synthesis because it can

263   form a dense protective layer on the nanoparticle surface, which stabilizes nanoparticles.[27]

264   A surface coating of BADGE aims to interface with the resin upon thermoset initiation. The

265   effect of CNP elemental ratio, additive loading, and magnetic field strength on the properties

266 are determined. Lap shear adhesion tests on industrially relevant substrates is performed.

267 Substrate and resin temperature during AMF exposure are independently determined through

268 fiber optic probes. Resin activation and propagation are characterized with thermogravimetric

269 analysis (TGA), dynamic scanning calorimetry (DSC), and infrared spectroscopy before and

270 after magnetocuring.

271

272 **3.1. XRD Confirms the Spinel Structure and Nano Crystalline Size of CNP.** The structural

273 determination of $Mn_xZn_{1-x}Fe_2O_4$, Curie nanoparticles are analyzed by the X-ray diffraction

274 patterns (**Figure 1A**), confirming the formation of cubic spinel structure for all the samples.

275 The experimental peaks are matched with JSPDS files and hkl planes are computed with Topas

276 software. The intense crystalline peaks observed at 2θ (hkl) value of 29.9 (220), 35.08 (311),

277 42.6 (400), 52.9 (422), 56.3 (511), and 61.9° (440) match the experimental data for the

278 franklinite spinel structure (JCPDS no. 10-0467), indicating the presence of $Mn_xZn_{1-x}Fe_2O_4$ in

279 all the samples. The small diffraction peak at 2θ of 33.61° is due to a small fraction of hematite

280 (α-Fe_2O_3) phase present in samples. The crystallite size of the particles was calculated using

281 the Scherrer formula ($D = 0.9\ \lambda/(\beta\ \cos\ \theta)$), the most intense diffraction peak at 2θ of 35.08°

282 corresponds to the plane 311. An increase in the Mn content results in an increase in crystallite

283 size of the particles. The crystallite size of $Mn_{0.4}$, $Mn_{0.5}$, $Mn_{0.6}$ and $Mn_{0.7}$ samples is found to

284 be 9.5, 13.5, 13.7 and 13.8 nm, respectively (**Figure 1B**).

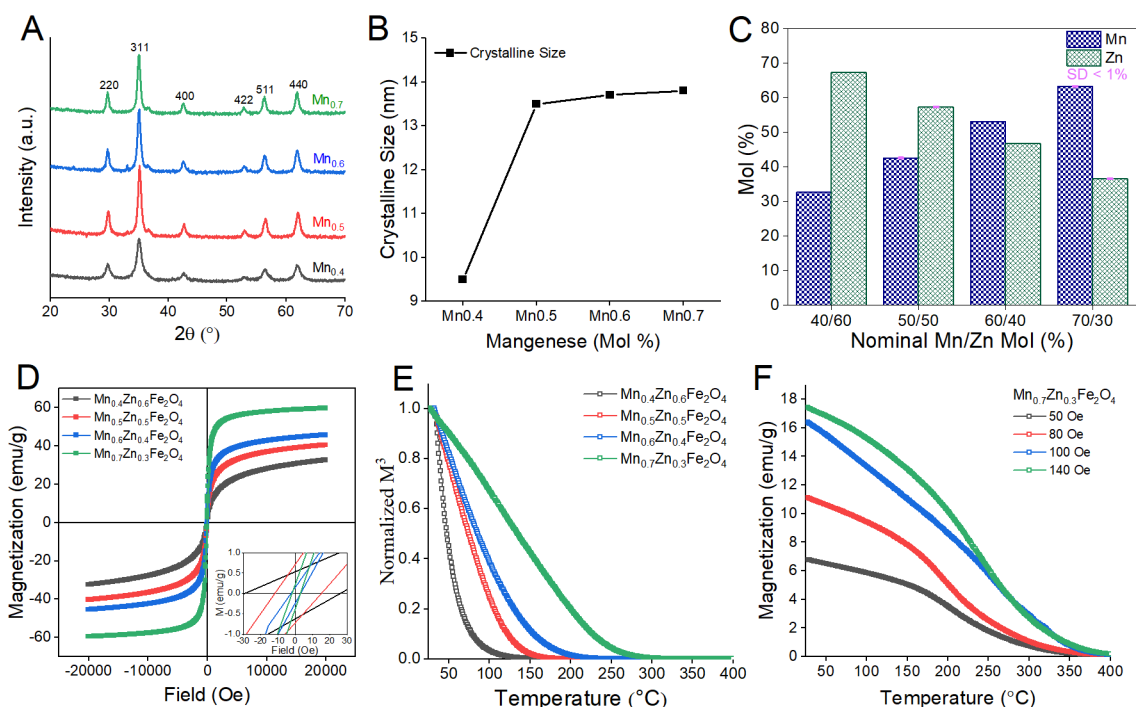**Figure 1.** Characterizations of curie nanoparticles (CNP). **A)** XRD analysis revealing spinel phase formation in $Mn_{0.4}Zn_{0.6}Fe_2O_4$ to $Mn_{0.7}Zn_{0.3}Fe_2O_4$. **B)** Scherrer equation estimated crystallite size of CNP. **C)** The actual composition of CNP measured by ICP-MS with standard deviation (SD) of < 1%. **D)** Magnetic hysteresis loops and cohesivity measured at room temperature using PPMS. **E)** Normalized magnetization as a function of temperature for $Mn_xZn_{1-x}Fe_2O_4$ CNP in the range from room temperature to 400 °C at a magnetic field of 140 Oe. **F)** Temperature dependence of magnetization for $Mn_{0.7}Zn_{0.3}Fe_2O_4$ CNP at applied magnetic fields of 50 Oe, 80 Oe, 100 Oe and 140 Oe.

3.2. The Actual Mn to Zn Ratio Differs by 9% to 18% from Feedstock Ratio. ICP-MS is employed to determine the Mn/Zn ratio of the four different $Mn_xZn_{1-x}Fe_2O_4$ compositions. In **Figure 1C**, the measured mol% ratios of manganese (Mn) and zinc (Zn) are presented as determined by ICP-MS and the results are compared to the nominal values. The ICP-MS results indicate that the actual mol fraction of $Mn_{0.4}$, $Mn_{0.5}$, $Mn_{0.6}$ and $Mn_{0.7}$ differ from the nominal compositions by 18%, 15%, 12% and 9%, respectively. Generally, the Zn cation gets uniformly distributed among the tetrahedral and octahedral sites.[28-30] Hence, it is expected that Mn^{+2} has a higher probability to get absorbed by a nucleus than Zn^{2+}. The smaller radius of Zn^{2+}

13

302   (0.74 Å) compared to Mn^{2+} (0.83 Å) might be the reason for an increased absorption of Zn^{2+}

303   into the lattice. The results also indicate that on increasing the Mn content, the difference

304   between the nominal and experimental values decreases. Incorporation of more Zn^{2+} ions is

305   observed for the lower Mn content particles ($Mn_{0.4}$).

306

307   **3.3. Magnetization and Curie temperature (Tc) Increases with Increasing Mn Content.**

308   The magnetic properties in ferrimagnetic spinels is mainly due to the super exchange

309   interaction mechanism between the metal ions in the A and B sublattices. The substitution of

310   non-magnetic Zn^{2+} ion, which prefers to occupy the A site, reduces the exchange interaction

311   between A and B sites. Hence, by varying the Mn/Zn ratio the magnetic properties of the CNP

312   can be tuned. **Figure 1D** presents the magnetization versus applied magnetic field curves

313   measured at room temperature. The saturation magnetization (M_s) of $Mn_{0.4}$, $Mn_{0.5}$, $Mn_{0.6}$ and

314    $Mn_{0.7}$ CNP is found to be 33 emu/g, 40 emu/g, 46 emu/g and 60 emu/g, respectively. All the

315   particles exhibit superparamagnetic behaviour with negligible hysteresis. The room

316   temperature coercivity (H_c) of all the samples are represented in the inset of **Figure 1D** and

317   **Table 2.** The H_c decreases with increasing Mn^{2+} content, down to a value of 2.4 Oe for $Mn_{0.7}$

318   particles**.** An increase of the Mn concentration in $Mn_xZn_{1-x}Fe_2O_4$ CNP leads to higher M_s. This

319   increase in M_s is due to the compositional change, the magnetic moments of Mn^{2+} (5 μ_B) ions

320   is higher than those of Fe^{2+} (4 μ_B) and Zn^{2+} (0 μ_B) ions. For the Curie temperature

321   measurements, the normalized temperature dependence of magnetization of CNP under an

322   applied magnetic field of 140 Oe is recorded in the temperature range from room temperature

323   to 400 °C **(Figure 1E)**. The CNP does not exhibit sharp transition at Curie temperature. Such

324   broad distribution of Curie temperature in fine magnetic nanoparticles is often observed. In

325   such cases, the spontaneous magnetization (M) scales as $(Tc–T)^\beta$ with a critical exponent, β =

326   1/3.[23, 31-33] Therefore, the M^3 is plotted with respect to temperature and Tc is determined

327 by extrapolating M^3 to zero.[31] The T_c of $Mn_{0.4}$, $Mn_{0.5}$, $Mn_{0.6}$ and $Mn_{0.7}$ is found to be 61 °C,

328 115 °C, 138 °C and 237 °C, respectively **(Figure 1E)**. This increase in T_c with increasing Mn

329 % in $Mn_xZn_{1-x}Fe_2O_4$ CNP is due to the enhanced total magnetic interactions within the unit

330 cell.[34] The temperature dependence of magnetization (M-T) for $Mn_{0.7}Zn_{0.3}Fe_2O_4$ is also

331 measured at different magnetic fields of 50 Oe, 80 Oe, 100 Oe and 140 Oe **(Figure 1F)**. The

332 magnetization at room temperature increases with increasing the magnetic field, consistent

333 with the higher AMF heating of these CNP at 140 Oe (more details will be discussed later).

334 The change in nature of M-T curves with applied magnetic field is because more thermal

335 energy is required to randomize the magnetic spin at high applied field.

336

337 **3.4. Low Temperature Magnetic Measurements Confirm the Superparamagnetic Nature**

338 **of CNP.** Zero field cooled (ZFC) and field cooled (FC) experiments are known to determine

339 the blocking temperature (T_B) of magnetic nanoparticles. In the ZFC measurements, the CNP

340 are cooled from 400 to 5 K in the absence of an applied magnetic field. After reaching 5 K, the

341 magnetization is determined as a function of increasing temperature under an external magnetic

342 field. For the FC measurements, the CNP are cooled from 400 to 5 K under an applied magnetic

343 field of 140 Oe. Subsequently, the magnetization is recorded in two modes; with increasing

344 temperature from 5 to 400 K which is known as field cooled warming (FCW) and with

345 decreasing temperature from 400 to 5 K referred as field cooled cooling (FCC).

346   **Figure 2A** depicts the ZFC, FCC and FCW magnetizations of all the CNP in the

347 temperature range of 5-400 K at an external magnetic field of 140 Oe. For all the samples, the

348 ZFC magnetization increases with the rising temperature and exhibits a broad maximum

349 centred at the blocking temperature (T_B). Such a peak temperature in the ZFC curves indicates

350 the transition from a magnetically blocked state at low temperatures to a superparamagnetic

351 state at higher temperatures. The T_B of $Mn_{0.4}$, $Mn_{0.5}$, $Mn_{0.6}$ and $Mn_{0.7}$ are found to 84, 125, 229

352 and 260 K, respectively, at magnetic field of 140 Oe, indicated by black vertical arrows in

353 **Figure 2A.** The shifting of T_B towards higher temperatures with increasing Mn content

354 $MnxZn_{1-x}Fe_2O_4$ is because of the strong magnetocrystalline anisotropy of Mn^{2+} ion.
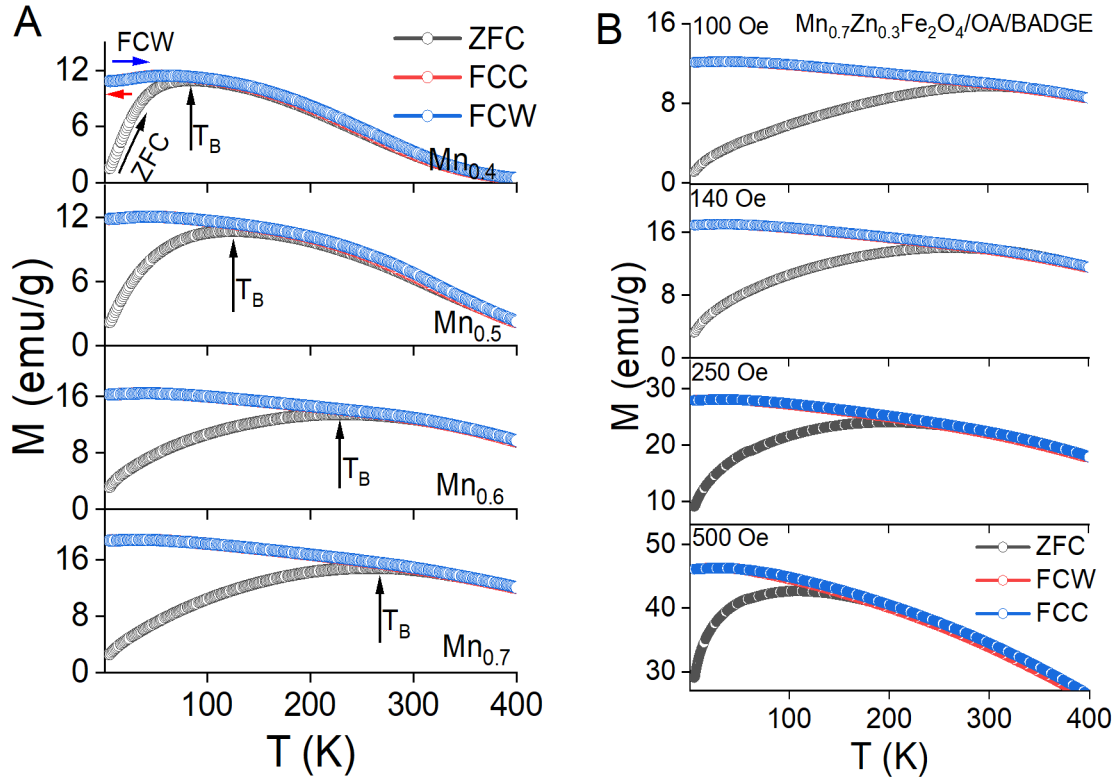

355

Figure 2. Low temperature magnetic characterizations of CNP **(A)** Zero field cooled (ZFC), field cooled cooling (FCC) and field cooled warmed (FCW) magnetization curves of $Mn_{0.4}$, $Mn_{0.5}$, $Mn_{0.6}$ and $Mn_{0.7}$ nanoparticles measured at an applied magnetic field of 140 Oe and temperature range of 5 K to 400 K. **(B)** ZFC, FCC and FCW magnetization curves of coated $Mn_{0.7}$ in the temperature range of 5 K to 400 K. at an applied magnetic field of 100 Oe, 140 Oe, 250 Oe and 500 Oe. Gray lines, red lines and the blue lines indicate the ZFC, FCC and FCW, respectively.

362

363 When CNPs are cooled to 5K without an external applied magnetic field, the net

364 magnetic moments of CNP align along their easy axis to obtain a local minimum of potential

365 energy.[35] The magnetic anisotropy of nanoparticles behaves as an energy barrier to keep the

366 magnetization direction in the easy axis. When the temperature increases from 5 K, the CNP

16

367 are thermally activated and starts to align along the external magnetic field which results in an

368 increase in magnetization with rising temperature. The magnetic anisotropy energy barrier

369 overcome by thermal energy at blocking temperature (T_B), leading to a superparamagnetic

370 state. Both FCW and FCC magnetization follow the same path and decrease with rising

371 temperature, they merge with the ZFC magnetization at the irreversible temperature (T_{ir}). T_{irr}

372 is related to the blocking of the larger (or agglomerated) particles in the system. Therefore, the

373 particle size distribution and degree of inhomogeneity can be qualitatively estimated from the

374 T_{irr}-T_B and the Mr/Ms.[36]   Higher values of T_{irr}-T_B and the Mr/Ms can lead higher

375 inhomogeneity. The magnetic characteristics of CNP are summarized in **Table 2**. The T_{irr} of

376 $Mn_{0.6}$ and $Mn_{0.7}$ are found to be 278 K and 300 K, respectively. **Figure 2B** shows the ZFC,

377 FCC and FCW magnetizations of coated $Mn_{0.7}$ for a range of external magnetic fields from 100

378 Oe to 500 Oe, and in the temperature range of 5-400 K. At applied magnetic field of 140 Oe,

379 the T_B, Tirr, and their difference (T_{irr}-T_B) of coated $Mn_{0.7}$ CNP exhibit lower values than those

380 of the corresponding uncoated particles, which can be associated with decreased attractive

381 forces between the coated CNP. It can also be noticed that both T_B and T_{irr} shift towards lower

382 temperature with an increase in applied magnetic field, which is characteristic of

383 superparamagnetic particles.[36]

384

385 **Table 2.** Magnetic characteristics of CNP ($Mn_xZn_{1-x}Fe_2O_4$)

Sample	H_c (Oe)	M_r (emu/g)	M_s (emu/g)	M_r/M_s	K* (10^3 J/m^3)	T_B (K)	T_{irr} (K)
$Mn_{0.4}$	27.6	0.534	33	0.01618	3.2	84	-
$Mn_{0.5}$	13.4	0.717	40	0.01793	4.7	125	-
$Mn_{0.6}$	2.8	0.156	46	0.00339	8.6	229	278

Mn$_{0.7}$	2.4	0.231	60	0.00385	9.8	260	300

386 *The effective anisotropy constant was calculated using the relation: $T_B = KV/25k_B$, where

387 T_B = blocking temperature, K = anisotropy constant, V = particles volume, k_B = Boltzmann

388 constant.

389 **3.5. Infrared Spectroscopy Confirms Oleic Acid and Epoxy Surface Functionalization.**

390 The functional groups present on CNP, oleic acid, BADGE and surface modifies CNP are

391 presented in **Figure 3A-3C**. The FT-IR spectra of bare Mn$_x$Zn$_{1-x}$Fe$_2$O$_4$ (x = 0.5, 0.6 and 0.7)

392 CNP have a sharp peak at 560 cm^{-1}, which corresponds to the characteristic features of ferrites

393 (Fe-O-Fe). Broad peaks at 3400 cm^{-1} and 1642 cm^{-1} also observed for the stretching vibrations

394 and H-O-H scissoring from free or absorbed hydroxide groups (**Figure 3A**).[37][38] **Figure**

395 **3B & 3C** indicates the FT-IR spectra of clean OA, BADGE, mixture of OA+BADGE and

396 Mn$_x$Zn$_{1-x}$Fe$_2$O$_4$/Oleic acid/BADGE (x =0.5, 0.6 and 0.7). Peaks for the presence of OA and

397 BADGE are observed to be very close and overlapped. The presence of oleic acid is confirmed

398 by the two sharp peaks at 2852 cm^{-1} and 2924 cm^{-1} for the symmetric and asymmetric stretching

399 vibrations of -CH$_2$ and -CH$_3$ **(Figure 3C).** The peaks at 1720 cm^{-1} and 1295 cm^{-1} are due to the

400 C=O and C-O stretching of the carboxylic group in oleic acid. Bending vibrations of C-H in

401 the methylene at 2962 cm^{-1} and 2927 cm^{-1} with the appearance of oxirane ring peaks at 830

402 cm^{-1} and 725 cm^{-1} confirms the BADGE functionalization.[39, 40]

403

404 **3.6. OA and BADGE Surface Functionalization Accounts for 20 *wt.%* CNP Mass.** The

405 amount of oleic acid and BADGE coated on the nanoparticles is determined by

406 thermogravimetric analysis. **Figure 3D and 3E** illustrates the TGA pattern of bare CNP and

407 Mn$_x$Zn$_{1-x}$Fe$_2$O$_4$/Oleic acid/BADGE, BADGE, OA and mixture of OA+BADGE, respectively.

408 A slight weight loss temperature below 150 °C in samples with and without coating could be

409 associated with water content **(Figure 3D)**. Oleic acid exhibits complete weight loss at 400 °C

410 while BADGE and mixture of OA + BADGE remains with some percentage of residue **(Figure**

411 **3E)**. The functionalized CNP exhibit two main weight loss stages between 150-500 °C and one

412 weight loss at higher temperature (> 500 °C). The first weight loss is associated with the

413 removal of physically absorbed OA and BADGE molecules from the surface of the CNP. The

414 second weight loss at 460 °C due to the strong binding force between CNP, OA and BADGE.

415 The third weight loss at ~750 °C is probably due to the complete decomposition of surfactant.

416 The total amount of OA+BADGE coating onto the CNP is found to be 23, 21 and 16 % (starting

417 weight % at room temperature - end weight % at 800 °C) for $Mn_{0.5}$, $Mn_{0.6}$ and $Mn_{0.7}$,

418 respectively.

419

420 **3.7. Colloidal Stability of Surface Modified CNP.** The colloidal stability of CNP is analyzed

421 using dynamic light scattering (DLS). Generally, an equilibrium between attractive forces

422 (magnetic dipole-dipole and Van der Waals) and repulsive forces (electrostatic and steric)

423 results in stability of nanoparticles.[41] Hence, bare CNP are less stable due to the low

424 electrostatic repulsive forces between them **(Figure S1, ESI).** The colloidal stability of the

425 functionalized CNP is determined by monitoring hydrodynamic size (**Figure 3F**). An optimum

426 size of 200-400 nm and count rate between ~300 to ~500 kcps is observed, confirming the
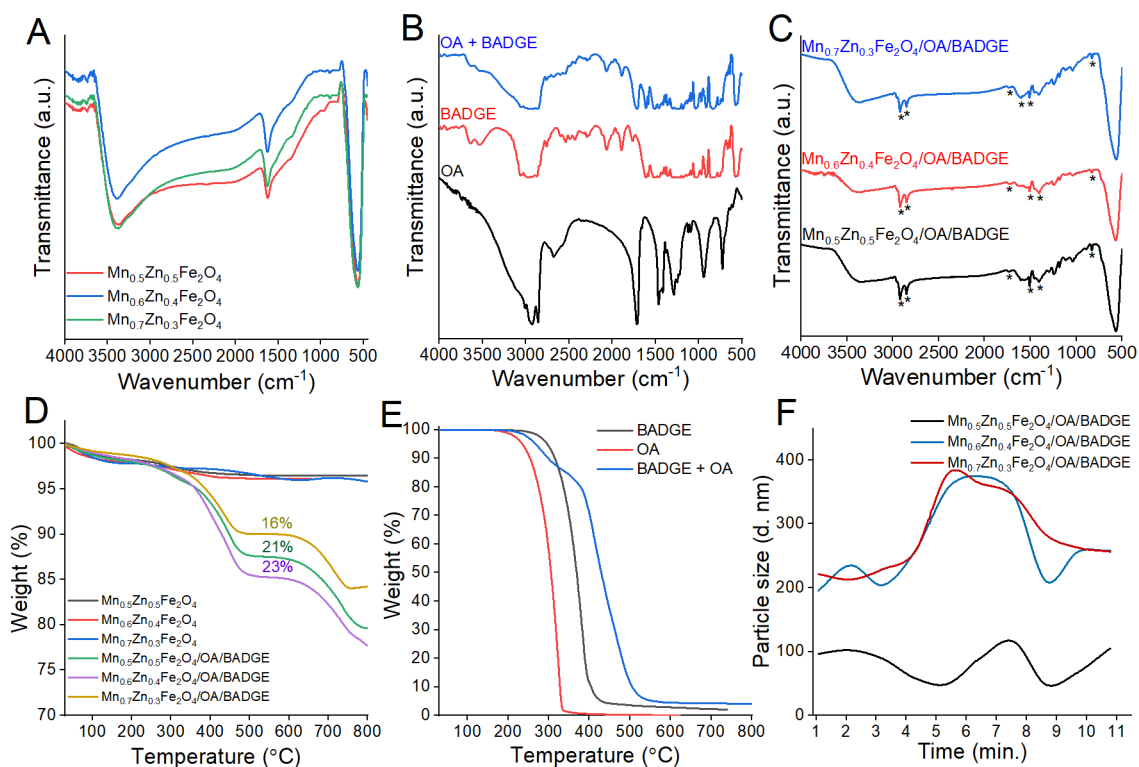
427 stability of CNP in ethanol.

Figure 3. Functionalization, surface modification and stability of curie nanoparticles. **A)** FT-IR spectra endorses the ferrite phase formation of $Mn_{0.5}Zn_{0.5}Fe_2O_4$, $Mn_{0.6}Zn_{0.4}Fe_2O_4$ and $Mn_{0.7}Zn_{0.3}Fe_2O_4$. **B)** Functional group representation of OA (oleic acid), BADGE (bisphenol A diglycidyl ether) and OA+BADGE. **C)** FT-IR spectra of OA and BADGE modified CNP (* represents the presence of OA and BADGE). **D)** Weight percent coating analyzed from the change in weight with temperature measured using TGA. **E)** Representation of thermal degradation pattern of clean OA, BADGE and OA+BADGE. **F)** DLS reveals the particle size stability with time of functionalized CNP in ethanol.

3.8. Transmission Electron Micrograph Endorses the Particle Size of Surface Functionalized $Mn_{0.7}$ from 9-25 nm.

The particles size and morphology of bare and coated $Mn_{0.7}$ particles are studied by TEM. **Figure 4** represents the TEM micrographs of bare and coated CNP and corresponding particle size distribution histograms. TEM images shows equiaxed individual particles with some agglomeration. The particle size of bare particles is in the range of 8 to 60 nm with an average particle size of 26 nm. The observed aggregation is

20

444   due to magnetic interactions between the particles and the absence of a surfactant layer. The

445   particle size of the coated particles is in the range of 9 to 25 nm, with an average particle size

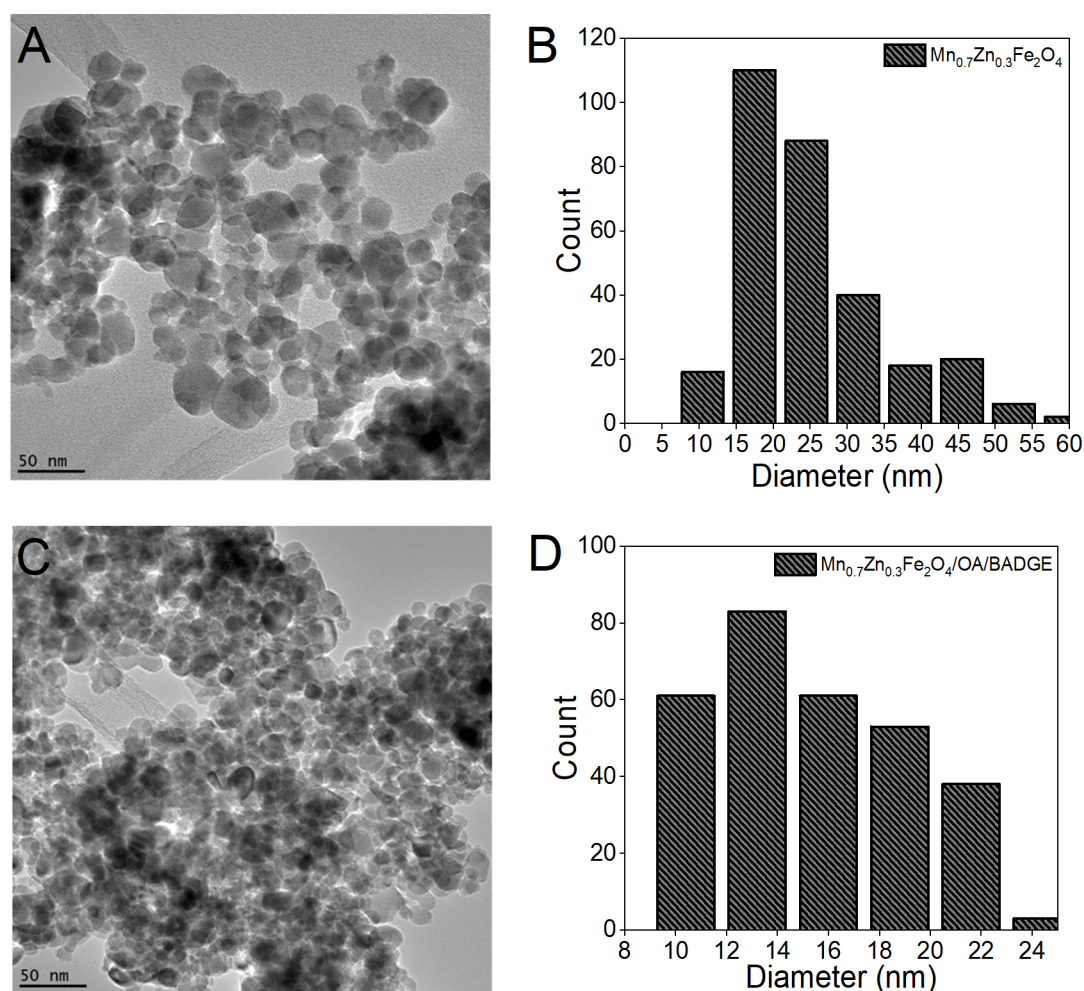446   of 16 nm, reasonably close to the value obtained from the XRD data (13.5 nm).

447

Figure 4. Transmission electron micrograph (TEM) and particle size distribution of (A-B)
$Mn_{0.7}Zn_{0.3}Fe_2O_4$ and (C-D) $Mn_{0.7}Zn_{0.3}Fe_2O_4$/OA/BADGE.

450

3.9. *In Situ* Heating of Epoxy Resins to 160 °C within 5 min. CNP serve as AMF-to-thermal

transducers to initiate thermosetting. To determine heating efficiency, functionalized CNP are

dispersed in BADGE using ultrasonication and the solution is then placed within the induction

coil at a frequency of 400 kHz and magnetic field strength ranging from 50 Oe to 140 Oe. The

heating efficiency depends strongly on AC magnetic field strength, *Tc* and CNP content in

456 BADGE. The temperature required for thermoset activation can be achieved within 5 min by

457 controlling the strength of the applied magnetic field. The temperature increases until a plateau

458 is reached at ~ 300 s. When magnetic nanoparticles suspended in an adhesive are subjected to

459 an AC magnetic field, losses from the cyclic reversal of magnetization results in a conversion

460 of electromagnetic energy to heat. The plateau temperature is a function of the AC magnetic

461 field strength and concentration of CNP in the adhesive. **Figure 5A-5D** depicts the temperature

462 versus time plots as a function of Mn/Zn ratio, percent loading, and field strength. The

463 maximum temperature (T_{max}) of $Mn_{0.7}Zn_{0.3}Fe_2O_4$/OA/BADGE is higher than the

464 corresponding values of $Mn_{0.5}Zn_{0.5}Fe_2O_4$/OA/BADGE, $Mn_{0.6}Zn_{0.4}Fe_2O_4$/OA/BADGE. In all

465 three cases, the high loading of CNP in BADGE results in a higher maximum temperature.

466 This maximum temperature is controlled by the Tc of the particles. The $Mn_{0.7}$ particles exhibit

467 the highest Tc (237 °C) and Ms (60 emu/g). A maximum temperature of 90 °C and 105 °C is

468 observed for $Mn_{0.5}$ and $Mn_{0.6}$ particles, respectively. The temperature can also be controlled by

469 tuning the AC magnetic field and time. **Figure 5D** depicts the AMF heating of

470 $Mn_{0.7}Zn_{0.3}Fe_2O_4$/OA/BADGE (15 *wt.%*) particles at field strengths ranging from 50 - 140 Oe.

471 The temperature of 48 °C, 90 °C, 118 °C and 134 °C correspond to AC magnetic fields of

472 50 Oe, 80 Oe, 100 Oe and 140 Oe, is achieved respectively. The maximum temperature is

473 reached within 10 min.. A maximum temperature of 140 °C and 160 °C is observed for 20 and

474 30 *wt.%* loading of $Mn_{0.7}$ particles in BADGE, respectively, at an AC field strength of 140 Oe.

475 The curing temperature of commercial thermoset adhesives (TIM 813-HTC and ES558) and

476 mixture of BADGE:DICY (100:12) are also within the range of 140 °C to 160 °C.[17, 42, 43]

477 Hence, $Mn_{0.7}Zn_{0.3}Fe_2O_4$/OA/BADGE formulation is selected. To prevent scorching/ hotspot

478 formation during adhesive curing, temperature and cure time is crucial. The AC field strength

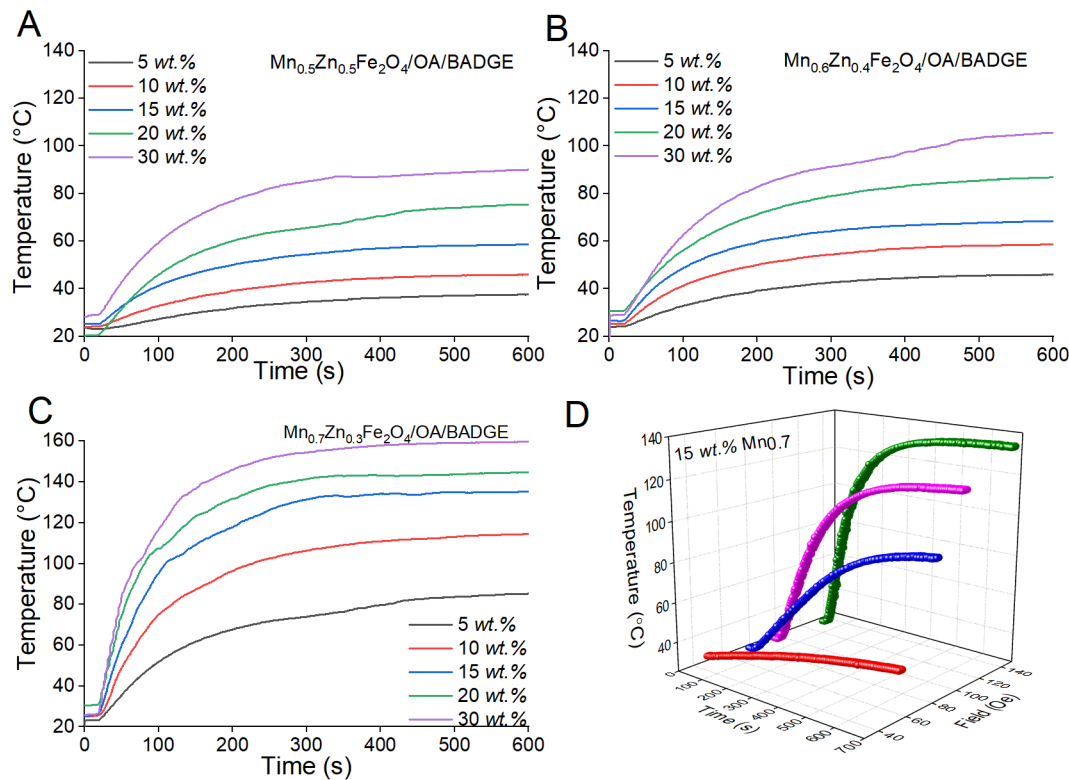479 and time can be selected to achieve the desired temperature.

Figure 5. Alternating magnetic field (AMF) heating curves for 5 - 30 *wt.%* loading of functionalized CNP into bisphenol A diglycidyl ether (BADGE) at 140 Oe. **A)** $Mn_{0.5}Zn_{0.5}Fe_2O_4/OA/BADGE$. **B)** $Mn_{0.6}Zn_{0.4}Fe_2O_4/OA/BADGE$. **C)** $Mn_{0.7}Zn_{0.3}Fe_2O_4/OA/$ BADGE. **D)** 15 *wt.%* $Mn_{0.5}Zn_{0.5}Fe_2O_4/OA/$ BADGE at AMF of 50, 80, 100 and 140 Oe.

3.10. Highest Specific Absorption Rate (SAR) of 5 Wg^{-1} is Achieved for $Mn_{0.7}Zn_{0.3}Fe_2O_4/OA/$ BADGE at 140 Oe.

The heating efficiency of the magnetic nanoparticles under AC magnetic field is defined by specific absorption rate (SAR) or specific loss power (SLP), expressed in Wg^{-1}.[44] SAR is defined as the amount of heat generated per unit mass of magnetic materials per unit time. It is calculated as per the Equation 1:

$$SAR = C_{solvent} \cdot m_{solvent} (dT/dt)/m_{CNP} \tag{1}$$

where $C_{solvent}$ is specific heat capacity of BADGE (346 J/mol K), m is the total mass of the solvent, m_{CNP} is the mass of the CNP and dT/dt is the temperature increase per unit time, that is, the initial slope of the temperature versus time curve. The average SAR value is calculated

23

495   for a range of loading of surface modified CNP. The temperature increase per time as a function

496   of CNP mass is represented in **Figure 6.** The SAR increases linearly with the magnetic field

497   amplitude and the highest SAR (5 Wg^{-1}) is observed for $Mn_{0.7}Zn_{0.3}Fe_2O_4$/OA/BADGE at 400

498   kHz frequency and 140 Oe amplitude because of the high M_s of these CNP. The SAR of

499    $Mn_{0.8}Zn_{0.2}Fe_2O_4$ at a frequency of 100 kHz and amplitude of 72 Oe was reported as low as 0.13

500   Wg^{-1}.[45] High SAR (57 Wg^{-1} (Mn + Fe)) is reported for $Mn_{0.62}Zn_{0.41}Fe_{1.97}O_4$ at higher

501   frequency of 970 kHz and field amplitude of 80 Oe.[46] SAR of ~ 7.5 to 10 Wg^{-1} of Mn-Zn

502   ferrite is also reported at different frequency and magnetic field strength of 520 kHz and 166

503   Oe.[47] It is concluded that SAR depends on several parameters, such as sample preparation

504   method, structural and magnetic properties of the nanoparticles, amplitude and frequency of

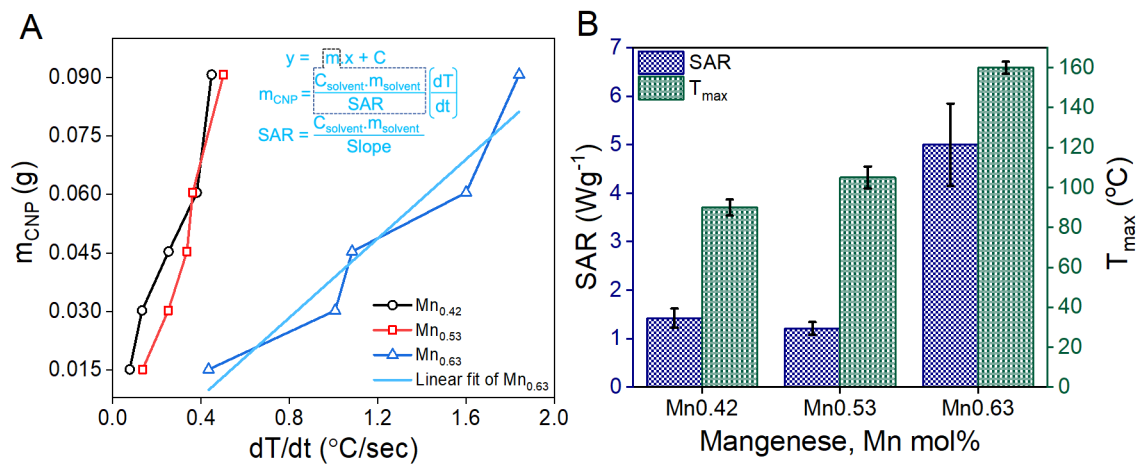505   the applied magnetic field, shape and size of nanoparticles, etc.[48-53]

506

507   **Figure 6.** Representation of specific adsorption rate (SAR) for $Mn_{0.5}Zn_{0.5}Fe_2O_4$/OA/BADGE ($Mn_{0.42}$),

508    $Mn_{0.6}Zn_{0.4}Fe_2O_4$/OA/BADGE ($Mn_{0.53}$) and $Mn_{0.7}Zn_{0.3}Fe_2O_4$/OA/ BADGE ($Mn_{0.63}$) **(A)** temperature

509   increase per second with mass of curie nanoparticles (m_{CNP}). **(B)** SAR with maximum AMF heating

510   (T_{max}) for different formulations.

511   **3.11. Magnetocuring Additive Cure Commercial Epoxy Adhesives.** A study of

512   magnetocuring of epoxy adhesives with loading of CNP (15, 20 and 30 *wt.%*) in Permabond

24

513   ES558, TIM 813-HTC or BADGE-DICY system to join various adherent materials (PMMA,

514   ABS, glass and wood) was performed. $Mn_{0.7}Zn_{0.3}Fe_2O_4$/OA/BADGE particles with an average

515   size of 14 nm are use due to their greater heating temperature range. The incorporation of

516   functionalized CNP into adhesives is done by hand mixing within the liquid thermoset resins.

517   The manufacture's recommended oven cure cycle is as follows: Permabond ES558; 75

518   min@130° C, 60 min@150 °C, or 40 min@170 °C.[54] TIM 813HTC; 1h@100 ºC+1h@150

519   ºC (recommended) or 30 min@150 ºC (alternate).[42] Control experiments of oven curing are

520   performed at 160 ºC for 1 h with a heating ramp rate of 10ºC/min.

521   Neat adhesives (ES558, TIM 813HTC and BADGE-DICY) are applied between the

522   ABS coupons (see **Figure 7A**) and determined as a negative control. With no magnetic

523   additives, there is no heating within the AMF coil. Next, epoxy/CNP magnetocuring additives

524   samples are placed within the induction coil, a rapid increase in temperature is observed. As

525   CNP are exposed to the AMF, heat dissipation takes place due to Neel and Brown relaxation

526   losses.[55-57]

527

528   **3.12. Steady Lap Shear Adhesion Strength is Optimized at 20-30% Loading.** After AMF

529   exposure, the samples are cooled to room temperatures and determined on a tensile tester under

530   lap-shear mode with a 500N load cell. A typical profile is displayed in **Figure 7B** with the

531   following formulation; 20 *wt.%* CNP+ES558 resin on ABS substrates. As **Figure 7C** shows,

532   loading % will affect the final temperature, epoxy crosslinking kinetics and lap shear adhesion.

533   ES558 thermoset with 15 and 20 *wt.%* magnetocuring additives displays a lap-shear strength

534   of 0.83 MPa, and 2 MPa, respectively, as shown in **Figure 7C**. Both thermosets TIM 813HTC

535   and BADGE-DICY (100:12) also bond ABS coupons to varying degrees (**Figure 7D**).

536   30 *wt.%* loading of CNP into ES558 is assessed against natural, plastic and glass

537   substrates typically found in industry (**Figure 7E**). The highest lap-shear strength is achieved

for wood (6.7 MPa) followed by glass (3.5 MPa), and plastics (<3 MPa), which roughly correlates to surface roughness and porosity. This does not represent the maximum adhesive bond, as the samples of plastic and wood have substrate failure modes. Glass displays interfacial debonding at the resin/substrate interface. Oven curing of ES558, TIM 813HTC and BADGE-DICY when compared to magnetocured samples displays little variation in lap shear strength for each product when magnetocuring is used (**Figure 7F**).
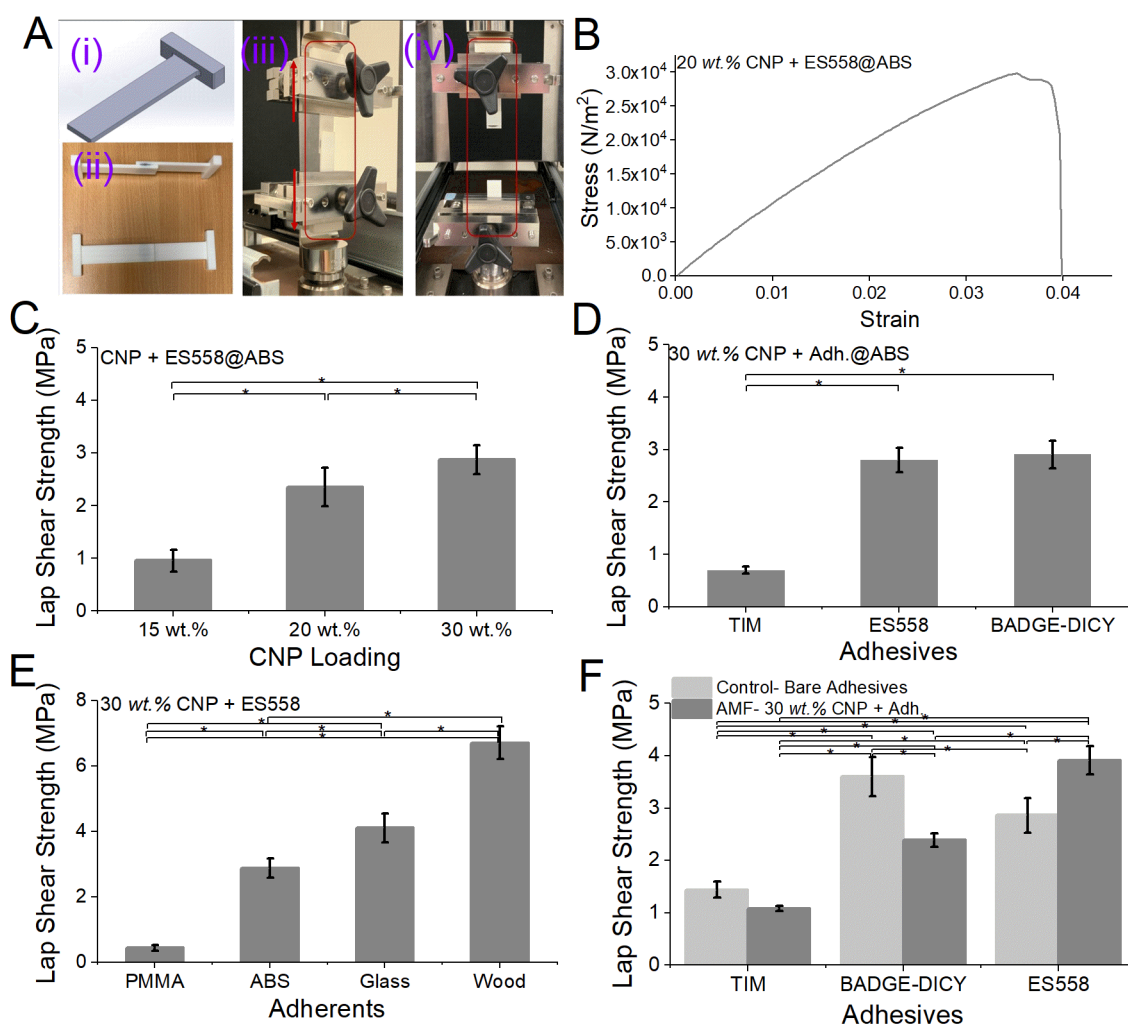

Figure 7. Mechanical and adhesion properties of commercial and homemade epoxy system. **A)** (i) Representation of digital model (CAD) used to print ABS coupons by 3D printer (ii) ABS coupons with magneto-adhesive cured under AMF (iii) Organised setup for mechanical test (iv) Bond/ABS breaking after mechanical test. **B)** Stress-strain curve of cured ES558@ABS with 20 *wt%* CNP. **C)** Lab shear adhesion strength of magneto-cured ES558@ABS with different loading of CNP.

550   **D)** Lab shear adhesion strength of different magneto-cured adhesives@ABS with 30 *wt.%* loading of

551   CNP. **E)** Lab shear adhesion strength of magneto-cured ES558 @ different adherent materials with 30

552   *wt.%* loading of CNP. **F)** Lab shear adhesion strength of oven and AMF cured adhesives@Glass. Data

553   presented as mean $\pm$ SD, n = 3 and significance is determined by one-way ANOVA, at $p < 0.05$.

554

555   **3.13. Curie Nanoparticles Provide Precise Temperature Control with No Scorching.**

556   Sample surface and thermoset resin temperatures are determined. Surface temperatures are

557   determined in real-time through a fibre optic thermocouple, internal thermoset resin

558   temperature is simultaneously determined with a fibre optic thermocouple and infrared camera.

559   **Figure 8A** show the surface temperature of four different substrates during magnetocuring of

560   ES558 with 20 *wt.%* loading of CNP. Surface temperature never exceeds 60-65 $^{\circ}$C for the 1-3

561   mm thick specimens, despite internal resin temperatures of 140 $^{\circ}$C (**Figure 8B).**   No

562   overheating is observed. Images captured by the FL-IR camera during AMF curing of 20

563   *wt.%* loaded ES558, also confirms the local heating.

564   Resin curing is further analysed by thermogravimetric analysis and dynamic scanning

565   calorimetry (DSC). Incomplete curing of the resin can be identified by the presence of a peak

566   at the activation temperature. **Figure 8C** displays the DSC spectra of uncured ES558 resin

567   (positive control) and magnetocured CNP composites. A single peak for the thermoset

568   activation temperature is observed at 150 $^{\circ}$C for the positive control but is absent in the

569   magnetocured composites. The overlapping TGA curves of thermocured *vs.* magnetocured

570   samples suggests no scorching of the magnetocured samples. A late peak after 500 $^{\circ}$C can be

571   seen in both clean and cured adhesive, which is due to oxidation and pyrolysis.

572

573   **3.14. Infrared Spectroscopy Indicates Epoxy Ring Opening and A Rigid Matrix.** The

574   degree of crosslinking in ES558 is qualitatively consistent with the infrared spectroscopy

575   results. **Figure 8D** compares uncured resin and the magnetocured CNP composites. Bending

576 vibrations of C-H in methylene (2923 cm^{-1}) and stretching vibrations of C=C in aromatic ring

577 (1602 and 1508 cm^{-1}) are both diminished, which is evidence of a rigid crosslinked resin. The

578 disappearance of the peaks at 915, 812 and 752 cm^{-1} indicates the opening of epoxy rings to

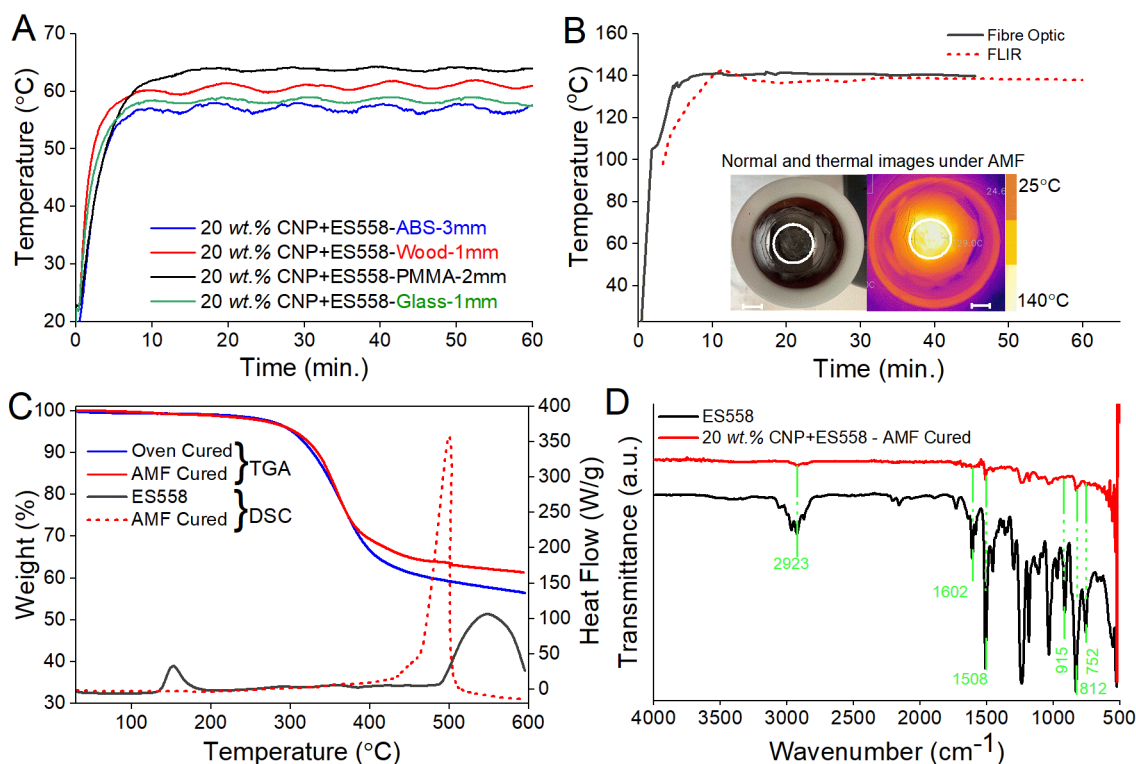579 form ether cross links.

580

581 **Figure 8. A)** Surface temperature during AMF curing @ different adherents. **B)** The temperature of

582 magnetoadhesive curing in AMF process measured by fibre optic thermocouple and FLIR camera (size

583 bar: 10 mm). **C)** TGA-DSC analysis of clean, oven and AMF cured ES558. **D)** FTIR-ATR spectra of

584 uncured ES558 and magnetocured CNP composite.

585

586 **4. Discussion**

587 A platform magnetocuring technology is developed to cure commercial thermoset resins via

588 exposure to alternating magnetic fields. The *in situ* thermal kinetics, particle loading, field

589 strength, and nature of the resins can be used to optimize performance of this technology.

590 Overheating prevention and colloidal stability in polar organic environments are advantages of

591   this technology. Previous demonstrations of magnetocuring adhesives observed resin

592   scorching due to runaway heating from a combination of particle-size dependent thermal

593   kinetics and agglomeration of metal oxide particles organic resins.[19-22, 58] The CNP

594   designed in the present work "switch off" above the Curie temperature, no feedback electronics

595   is required. The aggregation of high surface energy curie CNP, chemical reactivity and

596   dispersibility in solution was controlled by coating the CNP with functional shells of resin

597   based coatings for ease of dispersion. The coating is performed by post-synthesis grafting of

598   oleic acid on CNP *via* covalent bonds. The oleic acid coated particles are grafted with epoxy

599   monomers (BADGE) to improve thermoset initiation and like-dissolves-like particle

600   miscibility in one-component epoxy adhesives. The interaction of Fe^{3+} ions and hydroxyl

601   groups present at the surface of particles can interact with the polar groups of oleic acid and

602   BADGE, providing colloidal stability in epoxy.[59, 60] FT-IR spectra and TGA analysis

603   reveals the proper coating with oleic acid and BADGE onto the surface of particles. This may

604   be due to the interaction between oleic acid and BADGE **(Figure 3C).** Long-term colloidal

605   stability of functionalized CNP in BADGE was observed. Particles settled down after 1-2 h but

606   dispersed well again after sonication/ vortex for few min.

607   Heating in CNP arise from relaxation effects, i) the Brownian

608   mechanism of relaxation, in which the magnetic moment is locked to the crystal axis and

609   therefore the entire particle rotates with the magnetic field, ii) the Neel relaxation

610   mechanism, in which the magnetic moment rotates within the particle in an external magnetic

611   field.[60-63] ZFC-FC measurements confirm that the majority of the particles exhibit

612   superparamagnetic behaviour at room temperature. Moreover, $Mn_{0.7}$ particles, which were used

613   for magnetocuring, possess a low H_c (2.4 Oe), low M_r/M_s (0.0038) and CNP embedded in a

614   highly viscous/ solid matrix (adhesive). Therefore, the dominant heating mechanism should be

615   the result of relaxation processes, preferably Neels relaxation. The presence of nonzero

616 coercivity and nonzero M_r/M_s measured at room temperature can result in relatively small

617 hysteresis losses. Furthermore, the heating ability also depends on the properties of the

618 nanomaterials, such as particle size, magnetization and magnetic anisotropy, strength of

619 applied magnetic field (H) and frequency (f).[64, 65] Owing to the high Curie temperature and

620 magnetization of $Mn_{0.7}$ particles, highest heating of CNP was observed for the

621 $Mn_{0.7}Zn_{0.3}Fe_2O_4/OA/BADGE$ particles. In addition to high Ms and Tc, $Mn_{0.7}$ nanoparticles

622 exhibit higher magnetic moment than those of $Mn_{0.4}$, $Mn_{0.5}$ and $Mn_{0.6}$, revealed from

623 magnetization versus temperature curves at applied field of 100 and 140 Oe **(Figure S2, ESI).**

624 The SAR of these functionalized CNP dispersed in BADGE was found to be 5 Wg^{-1}. The

625 variation in SAR with mol % of Mn in $Mn_xZn_{1-x}Fe_2O_4$ might be due to the change in Ms and

626 therefore a notable change in the dipolar interparticle interactions. Further, the product of the

627 frequency and the magnetic field amplitude ($H \times f$) can decide whether the field/frequency is

628 in safe zone of medical application or not. Brezovich criterion sets a safety threshold to use

629 the AC magnetic field for human exposure by limiting the product of frequency and amplitude

630 to 5×10^8 $Am^{-1}s^{-1}$.[66] The use of high-frequency and high-amplitude AMF produce eddy

631 currents in conducting media which can results in nonspecific heating or damage the human

632 body. Other literature suggests that Hf factor should not be more than 5×10^9 $Am^{-1}s^{-1}$ for

633 medical applications, considering that smaller field exposure must be better tolerated by the

634 patients.[67] The maximum Hf for our system is 4.4 x 10^9 $Am^{-1}s^{-1}$, which suggest that curing

635 using the present approach can be applied for medical translation.

636   AMF heating of CNP results in crosslinking of one-component epoxy adhesives

637 through in situ heating. Complete curing of ES558 magnetoadhesive was achieved by applying

638 140 Oe of magnetic field strength for 1 h at a fixed frequency of 400 kHz. The structure activity

639 relationship were studied for different loading of CNP, adhesive systems, adherent and

640 controlled with oven-curing. The increase in the loading of CNP increases the shear strength

641 upto 3 MPa @ ABS. The increased shear strength was due to the interactions between the

642 curie nanoparticles and the adhesives. The interaction was facilitated by the presence of the

643 BADGE coating on the surface of curie nanoparticle. This results in greater stress transfer

644 between the curie nanoparticles and the matrix resulting in increased strength.

645   The strongest adhesion was observed for wood due to the pores on the wood surface.

646 The Magnetoadhesive can easily penetrate into the porous structure of wood during

647 magnetocuring process, which results in high lap shear strength. The maximum surface

648 temperature was less than 65 °C irrespective of the type of adherent, magnetocuring can locally

649 heat the joining part while preventing scorching.

650   A few of the limitations to scope and magnetocuring strategy should be noted.

651 Undeniably, magnetic properties of CNP are strongly depend on the synthesis procedures and

652 SAR values are mainly governed by the evaluating parameters like magnetic field amplitude,

653 frequency and CNP concentration. Due to the limitation of current AMF instrument, maximum

654 field of 140 Oe can be applied, which offers the SAR upto 5 Wg^{-1}. Although, high viscosity of

655 the media can be an another important considerable parameter as it will affect the heat

656 generation mechanism of CNP by Neel and Brown relaxations.[68, 69] These properties are

657 strongly speckled from one report to another. Furthermore, the current magnetocuring

658 approach is limited to the non-metallic substrates. The described oleic acid and epoxy

659 functionalized CNP are committed to the magnetocuring of one-component epoxy adhesives,

660 but it can also be further functionalized or decorated with various functional materials as per

661 the requirement. AMF heating results illustrates that the cap of magnetic field (140 Oe) and

662 frequency (400 kHz) ceases the heating of CNP below Curie temperature. Increase in the

663 magnetic field could leads to increase the AMF heating upto the Curie temperature control

664 point. In order to resolve these limitations, further scrutinizes will be focused on the magnetic

665 measurements of these CNP under AC magnetic field.

5. Conclusions

A series of $Mn_xZn_{1-x}Fe_2O_4$ nanoparticles were developed with a curie temperature range from 80 to 239 °C. Oleic acid/BADGE functionalized CNP dispersed well in BADGE and provided colloidal stability in epoxy and one-component epoxy adhesives. 20 - 30 *wt.%* loading of $Mn_{0.7}Zn_{0.3}Fe_2O_4$/OA/BADGE into ES558 was found to be suitable for magnetocuring of one-component epoxy adhesives without scorching. Mechanical testing results in a lap shear strength of upto 6.69 MPa for wood samples. The one-component magnetocuring adhesive allows us to develop or modify the existing formulations with CNP as filler/modifier. This technology is highly relevant to various applications in the field of sports, automotive and aerospace components and systems.

Declaration of Competing Interest

The authors declare no conflict of interest.

Acknowledgements

Supporting Information

Supporting Information is available with the online version of the paper.

References

[1]	https://www.marketwatch.com/press-release/instant-adhesive-market-2019-global-industry-size-growth-segments-revenue-manufacturers-and-2024-forecast-research-report-2019-09-03.
[2] A.M.G. Breifing, https://www.giiresearch.com/report/tbrc535848-traditional-adhesive-dressings-market-global.html, Business Research Company, (2017).

694 [3] S. Gillissen, E. Nelis, G.V. Wuytswinkel, M.D. Pater, C. Chih- Min, V. Buffa, W.O. Hara,
695 X. Bo, S. Jayesh, Low Temperature Snap Cure Thermoset Adhesives with Good Worklife., 5th
696 International Conference on Polymers and Adhesives in Microelectronics and Photonics,
697 IEEE, 2005, pp. 166−170.

698 [4] C. Dispenza, S. Alessi, G. Spadaro, Carbon Fiber Composites Cured by γ-Radiation-
699 Induced Polymerization of an Epoxy Resin Matrix, Adv. Polym. Technol. , 27 (2008) 163−171.

700 [5] X.K.D. Hillewaere, R.F.A. Teixeira, L.-T.T. Nguyen, J.A. Ramos, H. Rahier, F.E. Du Prez,
701 Autonomous Self-Healing of Epoxy Thermosets with Thiol-Isocyanate Chemistry, Advanced
702 Functional Materials, 24 (2014) 5575-5583.

703 [6] S. Rengasamy, V. Mannari, Development of Soy-Based UVCurable Acrylate ligomers and
704 Study of Their Film Properties, Prog. Org. Coat. , 76 (2013) 78−85.

705 [7] S.C. Ligon-Auer, M. Schwentenwein, C. Gorsche, J. Stampfl, R. Liska, Toughening of
706 Photo-Curable Polymer Networks: A Review, Polym. Chem., 7 (2016) 257−286.

707 [8] R. Rizzolo, D. Walczyk, J. Kuppers, Rapid Consolidation and Curing of Advanced
708 Composites with Electron Beam Irradiation., 30th Technical Conference of the American-
709 Society-for-Composites; Destech Publications, Inc.: Lancaster, (2015) 25−38.

710 [9] Mogal V, Papper V, Chaurasia A, Feng G, Marks R, T.W.J. Steele, Novel On-Demand
711 Bioadhesion to Soft Tissue in Wet Environments, Macromolecular bioscience, 4 (2014) 478-
712 484.

713 [10] J. Ping, F. Gao, J.L. Chen, R.D. Webster, T.W.J. Steele, Adhesive curing through low-
714 voltage activation, Nature Communications, 6 (2015) 1-9.

715 [11] V.T. Mogal, C.S. Yin, R. O'rorke, S. Boujday, C. Méthivier, S.S. Venkatraman, T.W.J.
716 Steele, Tuning model drug release and soft-tissue bioadhesion of polyester films by plasma
717 post-treatment, ACS Appied Materials and Interfaces 8(2014) 5749-5758.

718 [12] M. Singh, C.S. Yin, S.J. Page, Y. Liu, G. Wicaksono, R. Pujar, S.K. Choudhary, G.U.
719 Kulkarni, J. Chen, J.V. Hanna, R.D. Webster, Synergistic Voltaglue adhesive mechanisms with
720 alternating electric fields, Chemistry of Materials, 32 (2020) 2440-2449.

721 [13] J. Bauer, M. Bauer, Cyanate Ester Based Resin Systems for Snap Cure Applications,
722 Microsystem Technologies 8(2002) 58-62.

723 [14] A. Vitale, G. Trusiano, R. Bongiovanni, UV-curing of adhesives: a critical review,
724 Reviews of Adhesion and Adhesives, 2 (2017) 105-161.

725 [15] M. Laksin, Electron Beam Curing in Packaging-Challenges and Trends, RadTech Report
726 24, 2 (2010).

727 [16] J.G. Drobny, Radiation technology for polymers, CRC press, (2010).

728 [17] A. Pizzi, K.L. Mittal, Handbook of Adhesive Technology, Revised and Expanded: Taylor
729 & Francis, (2003).

730 [18] K.J. Miller, K.N. Collier, H.B. Soll-Morris, R. Swaminathan, M.E. McHenry, Induction
731 heating of FeCo nanoparticles for rapid rf curing of epoxy composites, Journal of Applied
732 Physics, 105 (2009).

733 [19] S. Ye, N.B. Cramer, B.E. Stevens, R.L. Sani, C.N. Bowman, Induction Curing of Thiol–
734 Acrylate and Thiol-Ene Composite Systems, Macromolecules, 44 (2011) 4988-4996.

735 [20] J.W. Hubbard, F. Orange, M.J. Guinel, A.J. Guenthner, J.M. Mabry, C.M. Sahagun, C.
736 Rinaldi, Curing of a bisphenol E based cyanate ester using magnetic nanoparticles as an
737 internal heat source through induction heating, ACS Appl Mater Interfaces, 5 (2013) 11329-
738 11335.

739 [21] W. Suwanwatana, S. Yarlagadda, J.W. Gillespie Jr, Hysteresis heating based induction
740 bonding of thermoplastic composites, Composites Science and Technology, 11-12 (2006)
741 1713-1723.

742 [22] M. Ma, Q. Zhang, J. Dou, H. Zhang, D. Yin, W.G. Zhou, Fabrication of one-dimensional
743 Fe3O4/P (GMA–DVB) nanochains by magnetic-field-induced precipitation polymerization,
744 Journal of colloid and interface science, 1 (2012) 339-344.
745 [23] A.S. Ahmed, R.V. Ramanujan, Curie temperature controlled self-healing magnet–polymer
746 composites, Journal of Materials Research, 30 (2015) 946-958.
747 [24] V. Chaudhary, Z. Wang, A. Ray, I. Sridhar, R.V. Ramanujan, Self pumping magnetic
748 cooling, Journal of Physics D: Applied Physics, 50 (2016).
749 [25] M.P. Edward, Epoxy adhesive formulations, McGrwa-Hill, New York 2006.
750 [26] R.A. Pethrick, Composite to metal bonding in aerospace and other applications, in: M.C.
751 Chaturvedi (Ed.) Welding and Joining of Aerospace Materials, Woodhead Publishing2012, pp.
752 288-319.
753 [27] R. Hao, R. Xing, Z. Xu, Y. Hou, S. Gao, S. Sun, Synthesis, Functionalization, and
754 Biomedical Applications of Multifunctional Magnetic Nanoparticles, Advanced Materials, 22
755 (2010) 2729-2742.
756 [28] A. Zapata, G. Herrera, Effect of zinc concentration on the microstructure and relaxation
757 frequency of Mn–Zn ferrites synthesized by solid state reaction, Ceramics International, 7
758 (2013) 7853-7860.
759 [29] R. Gimenes, M.D. Baldissera, M.R.A.D. Silva, C.A.D. Silveira, D.A.W. Soares, L.A.
760 Perazolli, M.R.D. Silva, M.A. Zaghete, Structural and magnetic characterization of MnxZn1−
761 xFe2O4 (x= 0.2; 0.35; 0.65; 0.8; 1.0) ferrites obtained by the citrate precursor method,
762 Ceramics international, 1 (2012) 741-746.
763 [30] I.C. Masthoff, A. Gutsche, H. Nirschl, G. Garnweitner, Oriented attachment of ultra-small
764 Mn (1-x)ZnxFe2O4 nanoparticles during the non-aqueous sol–gel synthesis, CrystEngComm,
765 12 (2015) 2464-2470.
766 [31] K.L. McNerny, Y. Kim, D.E. Laughlin, M.E. McHenry, Chemical synthesis of
767 monodisperse γ-Fe–Ni magnetic nanoparticles with tunable Curie temperatures for self-
768 regulated hyperthermia, Journal of Applied Physics, 107 (2010).
769 [32] A. Belayachi, J.L. Dormann, M. Noguès, Critical analysis of magnetically semi-disordered
770 systems: critical exponents at various transitions, Journal of Physics: Condensed Matter, 10
771 (1998) 1599-1619.
772 [33] K. Fabian, V.P. Shcherbakov, S.A. McEnroe, Measuring the Curie temperature,
773 Geochemistry, Geophysics, Geosystems, 14 (2013) 947-961.
774 [34] R. Arulmurugan, G. Vaidyanathan, S. Sendhilnathan, B. Jeyadevan, Mn–Zn ferrite
775 nanoparticles for ferrofluid preparation: Study on thermal–magnetic properties, Journal of
776 Magnetism and Magnetic Materials, 298 (2006) 83-94.
777 [35] C. Murugesan, G. Chandrasekaran, Structural and Magnetic Properties of
778 Mn1−xZnxFe2O4 Ferrite Nanoparticles, Journal of Superconductivity and Novel Magnetism,
779 29 (2016) 2887-2897.
780 [36] S. Dey, R. Mondal, S.K. Dey, S. Majumder, P. Dasgupta, A. Poddar, V.R. Reddy, S.
781 Kumar, Tuning magnetization, blocking temperature, cation distribution of nanosized
782 Co0.2Zn0.8Fe2O4 by mechanical activation, Journal of Applied Physics, 118 (2015) 103905.
783 [37] R.D. Waldron, Infrared spectra of ferrites, Physical Review, 99 (1955) 1727–1735.
784 [38] M. Kaiser, Effect of preparation condition on nickel zinc ferrite nanoparticle: a
785 comparison between sol-gel, Journal of Alloys and Compounds, 468 (2009) 15-21.
786 [39] M.G. González, J.C. Cabanelas, J. Baselga, Applications of FTIR on epoxy resins-
787 identification, monitoring the curing process, phase separation and water uptake, Infrared
788 Spectroscopy-Materials Science, Engineering and Technology, 2 (2012) 261-284.
789 [40] E.V. Barreiro, F.F. López, A. Jover, F. Meijide, E. Rodríguez, J.V. Tato, Paramagnetic
790 epoxy resin, eXPRESS Polymer Letters, 11 (2017) 60.

791 [41] I. Sharifi, H. Shokrollahi, S. Amiri, Ferrite-based Magnetic Nanofluids Used in
792 Hyperthermia Applications, Journal of Magnetism and Magnetic Materials, 324 (2012) 903-
793 915.
794 [42] TIMTRONICS 813HTC, https://timtronics.com/wp-content/uploads/2018/03/TIM-
795 813HTC_TDS.pdf.
796 [43] Permabond ES558, https://www.permabond.com/wp-
797 content/uploads/2016/04/ES558_TDS.pdf, (25 October 2019).
798 [44] G. Cotin, F. Perton, C. Blanco-Andujar, B. Pichon, D. Mertz, S. Bégin-Colin, Design of
799 Anisotropic Iron-Oxide-Based Nanoparticles for Magnetic Hyperthermia. In Nanomaterials for
800 Magnetic and Optical Hyperthermia Applications, Elsevier2019.
801 [45] T.M. Elkhova, A.K. Yakushechkina, A.S. Semisalova, Y.K. Gun'ko, Y.I. Spichkin, A.P.
802 Pyatakov, K.I. Kamilov, N.S. Perov, A.M. Tishin, Heating of Zn-substituted manganese ferrite
803 magnetic nanoparticles in alternating magnetic field, Solid State Phenomena, Trans Tech
804 Publications Ltd., 233 (2015) 761-765.
805 [46] J. Stergar, Z. Jirák, P. Veverka, L. Kubíčková, T. Vrba, J. Kuličková, K. Knížek, F.
806 Porcher, J. Kohout, O. Kaman, Mn-Zn ferrite nanoparticles coated with mesoporous silica as
807 core material for heat-triggered release of therapeutic agents, Journal of Magnetism and
808 Magnetic Materials, 475 (2019) 429-435.
809 [47] A. Jordan, P. Wust, H. Fählin, W. John, A. Hinz, R. Felix, Inductive heating of
810 ferrimagnetic particles and magnetic fluids: physical evaluation of their potential for
811 hyperthermia, International Journal of Hyperthermia, 1 (1993) 51-68.
812 [48] E. Kita, T. Oda, T. Kayano, S. Sato, M. Minagawa, H. Yanagihara, M. Kishimoto, C.
813 Mitsumata, S. Hashimoto, K. Yamada, N. Ohkohchi, Ferromagnetic nanoparticles for magnetic
814 hyperthermia and thermoablation therapy, Journal of physics D: Applied physics, 43 (2010)
815 474011.
816 [49] P. De la Presa, Y. Luengo, M. Multigner, R. Costo, M.P. Morales, G. Rivero, A. Hernando,
817 Study of heating efficiency as a function of concentration, size, and applied field in γ-Fe2O3
818 nanoparticles, The Journal of Physical Chemistry C, 116 (2012) 25602-25610.
819 [50] M.A. Gonzalez-Fernandez, T.E. Torres, M. Andrés-Vergés, R. Costo, P. De la Presa, C.J.
820 Serna, M.P. Morales, C. Marquina, M.R. Ibarra, G.F. Goya, Magnetic nanoparticles for power
821 absorption: Optimizing size, shape and magnetic properties, Journal of Solid State Chemistry,
822 182 (2009) 2779-2784.
823 [51] N.K. Prasad, K. Rathinasamy, D. Panda, D. Bahadur, Mechanism of cell death induced by
824 magnetic hyperthermia with nanoparticles of γ-Mn x Fe 2–x O 3 synthesized by a single step
825 process, Journal of Materials Chemistry, 17 (2007) 5042-5051.
826 [52] C. Martinez-Boubeta, K. Simeonidis, A. Makridis, M. Angelakeris, O. Iglesias, P.
827 Guardia, A. Cabot, L. Yedra, S. Estradé, F. Peiró, Z. Saghi, Learning from nature to improve
828 the heat generation of iron-oxide nanoparticles for magnetic hyperthermia applications. ,
829 Scientific reports, 3 (2013) 1652.
830 [53] Y. Piñeiro-Redondo, M. Bañobre-López, I. Pardiñas-Blanco, G. Goya, M.A. López-
831 Quintela, J. Rivas, The influence of colloidal parameters on the specific power absorption of
832 PAA-coated magnetite nanoparticles, Nanoscale research letters, 6 (2011) 383.
833 [54] Permabond ES558, https://www.permabond.com/wp-
834 content/uploads/2016/04/ES558_TDS.pdf,, (25 October 2019).
835 [55] L. Néel, Influence of thermal fluctuations on the magnetic after-effect of solid
836 ferromagnetics in the Rayleigh region, J. Phys. Radium, 11 (1950) 49-61.
837 [56] W.F. Brown Jr, Thermal fluctuations of a single-domain particle, Physical Review, 130
838 (1963) 1677.

839 [57] K.L. McNerny, Y. Kim, D.E. Laughlin, M.E. McHenry, Chemical synthesis of
840 monodisperse γ-Fe–Ni magnetic nanoparticles with tunable Curie temperatures for self-
841 regulated hyperthermia, Journal of Applied Physics, 9 (2010) 09A312.
842 [58] K.J. Miller, K.N. Collier, H.B. Soll-Morris, R. Swaminathan, M.E. McHenry, Induction
843 heating of FeCo nanoparticles for rapid rf curing of epoxy composites, Journal of Applied
844 Physics, 105 (2009) 07e714.
845 [59] W. Wang, C. Zang, Q. Jiao, Wear-resistant and electromagnetic absorbing behaviors of
846 oleic acid post-modified ferrite-filled epoxy resin composite coating, Journal of Magnetism
847 and Magnetic Materials, 378 261-266.
848 [60] R.E. Rosensweig, Heating magnetic fluid with alternating magnetic field, Journal of
849 magnetism and magnetic materials, 252 (2002) 370-374.
850 [61] V. Chaudhary, Y. Zhong, H. Parmar, V. Sharma, X. Tan, R.V. Ramanujan,
851 Mechanochemical synthesis of iron and cobalt magnetic metal nanoparticles and iron/calcium
852 oxide and cobalt/calcium oxide nanocomposites, ChemistryOpen, 8 (2018) 590-598.
853 [62] P. Lemal, S. Balog, L. Ackermann-Hirschi, P. Taladriz-Blanco, A.M. Hirt, B. Rothen-
854 Rutishauser, M. Lattuada, A. Petri-Fink, Simple and fast evaluation of relaxation parameters
855 of magnetic nanoparticles, Journal of Magnetism and Magnetic Materials, 499 (2020) 166176.
856 [63] M.N. Halgamuge, T. Song, Optimizing Heating Efficiency of Hyperthermia: Specific Loss
857 Power of Magnetic Sphere Composed of Superparamagnetic Nanoparticles, Progress In
858 Electromagnetics Research, 87 (2020) 1-17.
859 [64] C. Martinez-Boubeta, K. Simeonidis, A. Makridis, M. Angelakeris, O. Iglesias, P.
860 Guardia, A. Cabot, L. Yedra, S. Estrade, F. Peiro, Z. Saghi, Learning from nature to improve
861 the heat generation of iron-oxide nanoparticles for magnetic hyperthermia applications, Sci.
862 Rep. , 3 (2013) 1652.
863 [65] R. Kappiyoor, M. Liangruksa, R. Ganguly, I.K. Puri, The effects of magnetic nanoparticle
864 properties on magnetic fluid hyperthermia, J. Appl. Phys., 108 (2010) 094702.
865 [66] I.A. Brezovich, Low frequency hyperthermia: capacitive and ferromagnetic thermoseed
866 methods, Medical physics monograph, 16 (1988) 82-111.
867 [67] R. Hergt, S. Dutz, Magnetic particle hyperthermia-biophysical limitations of a visionary
868 tumour therapy, Journal of Magnetism and Magnetic Materials, 311 (2007) 187-192.
869 [68] S. Bae, S.W. Lee, Y. Takemura, Applications of Ni Fe2O4 nanoparticles for a
870 hyperthermia agent in biomedicine, Applied physics letters, 89 (2006) 252503.
871 [69] E.Y.K. Ng, S.D. Kumar, Physical mechanism and modeling of heat generation and transfer
872 in magnetic fluid hyperthermia through Néelian and Brownian relaxation: a review,
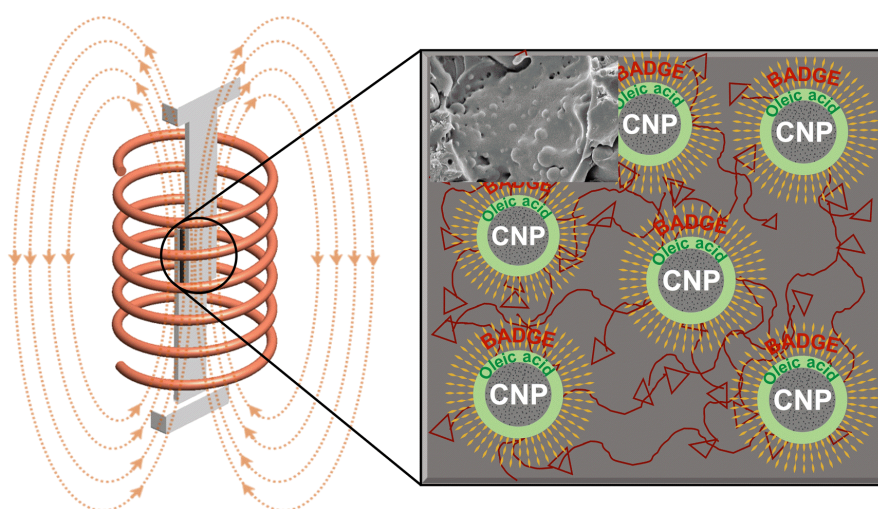873 Biomedical engineering online, 16 (2017) 36.

874

Magnetocuring of Temperature Failsafe Epoxy Adhesives

Richa Chaudhary, Varun Chaudhary, Raju V. Ramanujan, Terry W. J. Steele

School of Materials Science and Engineering (MSE), Division of Materials Technology, Nanyang Technological University (NTU), Singapore 639798

Corresponding author: Terry W. J. Steele (e-mail: wjsteele@ntu.edu.sg)

Graphical abstract:

Magnetocuring : On-demand adhesion

Magnetocuring of Temperature Failsafe Epoxy Adhesives

Richa Chaudhary, Varun Chaudhary, Raju V. Ramanujan, Terry W. J. Steele

School of Materials Science and Engineering (MSE), Division of Materials Technology, Nanyang Technological University (NTU), Singapore 639798

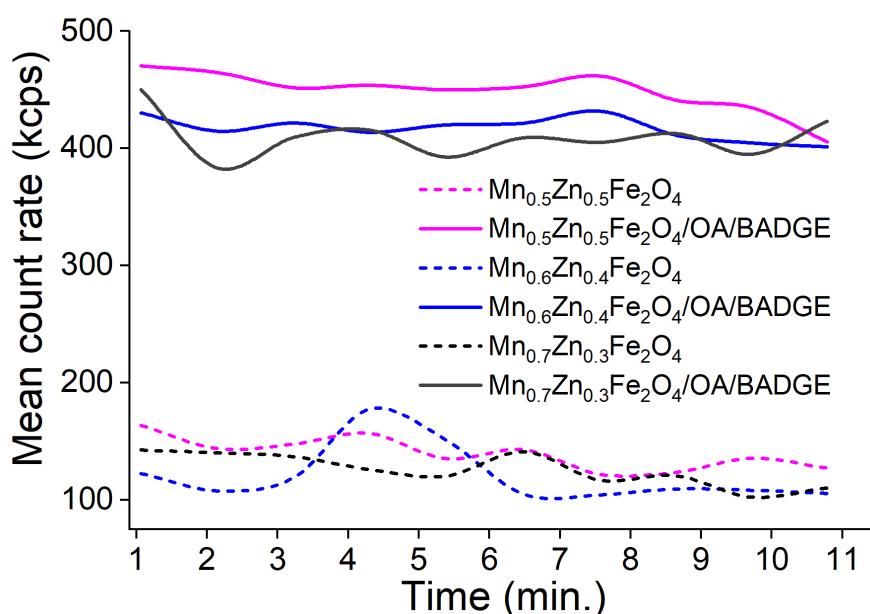Corresponding author: Terry W. J. Steele (e-mail: wjsteele@ntu.edu.sg)

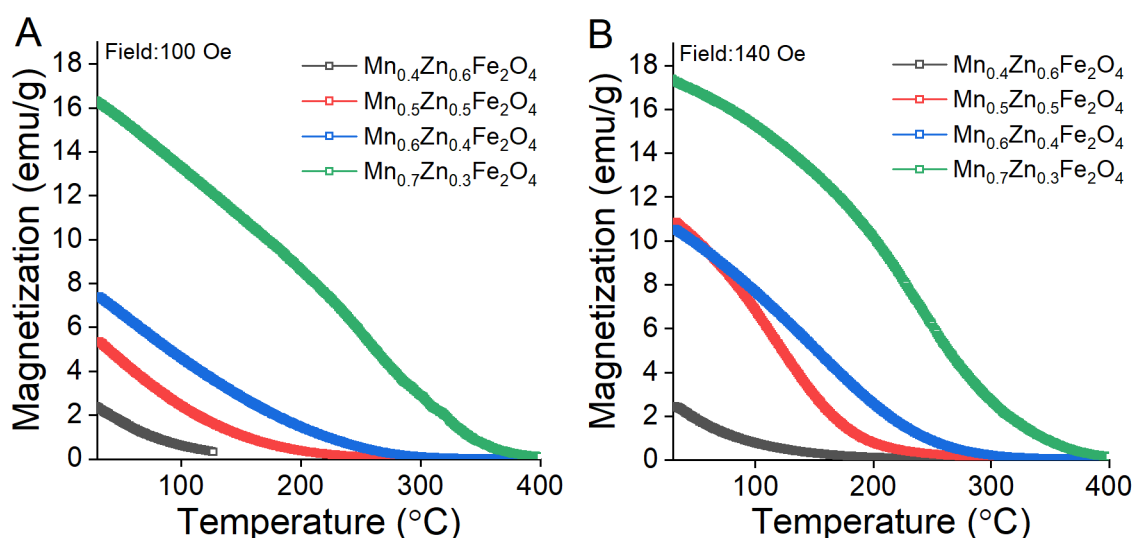**Figure S1.** DLS confirms the colloidal stability of functionalized CNPs in ethanol.

Figure S2. Magnetization as a function of temperature for $Mn_xZn_{1-x}Fe_2O_4$ CNPs at different magnetic field **(A)** 100 and **(B)** 140 Oe.